{Citation}Article Draft

Rainfall extremes under future climate change with implications for urban flood risk in Kathmandu, Nepal

Dibesh Shrestha[1,2], Divas B. Basnyat[1,2], Januka Gyawali[3], Maggie J. Creed[4], Hugh D. Sinclair[5], Brian Golding[6], Manoranjan Muthusamy[7], Shankar Shrestha[2], C. Scott Watson[8], Divya L. Subedi[2], Rojina Haiju[2]

Abstract:

Increased rainfall extremes cause severe urban flooding in cities with adverse socio-economic consequences, and Kathmandu city is no exception. Rainfall events are projected to become more intense and frequent in a warm and wet future, and they pose a major challenge to the sustainable development of Kathmandu city. This paper analyses historical extreme rainfall patterns across the city and uses these as the basis for future projections in combination with a range of General Circulation Models. Future projections of extreme rainfall are then fed into the numerical flood model HAIL-CAESAR (Lisflood), using a high-resolution digital elevation model of Kathmandu. We show that rainfall intensity, such as the 24-hour maximum rainfall (RX1day), is projected to increase by up to 72% in the future, and the historical 100-year return period rainfall will become a 20 or 25-year return period rainfall. The flood modelling results show that the future flood hazard (magnitude and extent) will increase. The historical 100-year return period flood discharge will correspond to a 25-year return period future flood. A 100-year period flood discharge is likely to increase up to 72% (37% median) in the future. Area of land inundated by more than 1 m in a 100-year return period flood event could increase from 11.7 km² to 23 km² in the future. Furthermore, the location and timing of rainfall maxima affect the peak, timing, and location of flood hazards. This analysis can serve as a scientific basis to assess future flood-induced risk in Kathmandu in response to climate change.

Keywords: Rainfall extreme, Kathmandu, climate change, urban flood, RX1day rainfall, Lisflood

1 Introduction

Urban flood risk management is integral to climate-resilient urban development as more people are predicted to live in urban areas (IPCC, 2022). Climate-related extremes are projected to be more frequent and intense with temperature rise (AghaKouchak et al., 2020; Alfieri et al., 2017). The increasing trend of heavy precipitation events has already resulted in recurrent and severe urban flooding in cities across the globe (Dodman et al., 2022). Climate change is expected to exacerbate this condition further. It is estimated that without adaptation, direct flood damages are projected to

[1] Corresponding authors: dibeshshrestha@live.com and divas@ndri.org.np
[2] Water and Climate Program, Nepal Development Research Institute (NDRI), Lalitpur, Nepal
[3] Practical Action, Kathmandu, Nepal
[4] James Watt School of Engineering, The University of Glasgow, Glasgow G12 8QQ, UK
[5] School of GeoSciences, The University of Edinburgh, Drummond Street, Edinburgh EH8 9XP, UK
[6] Met Office, Exeter, Devon EX1 3PB, UK
[7] FloodFlash, London E1 5LN, UK
[8] COMET, School of Earth and Environment, University of Leeds, LS2 9JT, UK

increase by 1.4 to 2 times at a 2°C global temperature rise compared to a 1.5°C temperature rise (IPCC, 2022).

Nepal is one of the countries most vulnerable to river flood hazards in the world (Alfieri et al., 2017). In the last decade, intense rainfall and consequent floods have caused displacement of people, infrastructure damages and disruption of urban services (Ojha, 2021; Ojha and Dhungana, 2021; Uprety, 2019). Examples of these increasing urban flood risks include the major flood events in July 2014, August 2018, July 2019 and September 2021. As agricultural land is rapidly converted into urban settlements in Kathmandu (Lamichhane and Shakya, 2019; Shrestha and Acharya, 2021), the increase in flood-plain urbanisation, river encroachment, and channelisation of the existing river and tributaries will increase exposure and vulnerability of urban infrastructure and settlements to flood hazards.

Future cities need to be prepared for the evolving risks associated with flood hazards in the context of the changing climate, and meaningful quantification of future flood risks is required to inform the risk-sensitive design of tomorrow's cities (Cremen et al., 2022). Climate-resilient design also means addressing the uncertainty related to climate change and variability, which the current regime of infrastructure design processes lacks because of its inherent assumption that the future will look like the present (Brown et al., 2020).

However, quantifying the impact of climate change on flood hazards is challenging (Brunner et al., 2021). Global Climate Models (GCMs) are used to force the hydrological simulation required to estimate future flood projections. However, there is uncertainty associated with estimating and projecting precipitation extremes. Some limitations of climate models include spatial resolution (coarser resolution) (Fowler et al., 2007; Teutschbein and Seibert, 2012), hydrologic process representation (Clark et al., 2015), sub-grid parameterisation (Yin et al., 2023), and model initialisation (Richter et al., 2020). These limitations lead to biases in GCMs results. Therefore, using climate models in a local context requires data processing such as statistical downscaling and bias correction (Fowler et al., 2007; Hakala et al., 2019; Teutschbein and Seibert, 2012). The wide spread of predictions in GCMs is a major source of uncertainty in climate impact studies compared to other sources of uncertainties such as parametric or hydrological model structure uncertainties (Finger et al., 2012; Minville et al., 2008). It is thus necessary to incorporate the uncertainties associated with GCMs into future flood hazard and risk analysis. Uncertainties can be incorporated into the analysis using a selection of plausible representative climate futures (e.g., Whetton et al., 2012) or an envelope-based approach (e.g. Lutz et al., 2016). Following the envelope-based approach of Lutz et al. (2016), GCMs are selected based on their future projections of average climatic changes, modifications in climate extremes, and their ability to simulate past climate accurately. The method encompasses a wide range of possible changes in precipitation and temperature in the future and categorises them into four futures: cold-wet, cold-dry, warm-wet and warm-dry conditions. This provides a basis for evaluating vulnerabilities of a water system (such as flood protection or irrigation) in the given conditions and quantifies the uncertainty range required for decision making.

To effectively assess climate risks, a context-based, bottom-up approach is necessary (Mendoza et al., 2018; Ray and Brown, 2015). It begins by analysing the climate conditions that lead to high-impact vulnerabilities or hazards. The envelope approach, using selected GCMs, provides the necessary climate conditions for assessing potential future flood hazards. The Tomorrow's Cities Decision Support Environment (TCDSE) recognises the importance of simulating multiple-hazard scenarios and their consequences as a key element in preparing for future risks (Galasso et al., 2021; Cremen et al., 2023). Jenkins et al. (2023) under TCDSE has implemented the "Multi-hazard modelling", with simulations of flood, earthquake, and debris flow scenarios, in assisting with the identification of developing urban regions that are vulnerable to potential multi-hazard events. The methodology adopted in this study aligns with the process of estimating future flood risks associated with different scenarios and incorporating these into the climate-resilient design of urban spaces in Kathmandu, as described in Cremen et al. (2022).

Our approach starts with the diagnostic analysis of high-impact historical extreme precipitation and flood events to analyse the climate drivers, extreme precipitation indices and patterns of urban flooding in the Kathmandu basin. This specific context-based information is then used to bias correct and downscale the GCM projections of the extreme precipitation (RX1Day, One-day Maximum Rainfall) to the required spatial and temporal scale required for flood modelling in the Kathmandu valley. To align the concept of climate change driven future precipitation events with the traditional engineering approach for categorising flood events, we express the rainfall and floods in terms of their probabilities or return period. The rationale and motivations of the methodology used in this paper are based on the realisation that the future climate will differ from the past, but the information and knowledge of the historical high-impact extreme precipitation and flood events are useful in addressing some of the limitations of future climate projections. Thus, the main objective of the paper is to analyse and use the temporal and spatial variations of high-impact precipitation events of the past to define the extreme precipitation under climate change and then assess future flood-induced impacts in Kathmandu. This paper presents a workflow for assessing future flood hazards that integrates various established approaches such as GCM selection, spatial analysis of rainfall, non-stationary rainfall frequency analysis, spatial disaggregation of rainfall based on historical extreme event and hydrodynamic modelling. To overcome the lack of observed sub-daily precipitation data, we combine the historical observed spatially distributed rainfall data with the temporal distribution of satellite-based rainfall data to obtain a spatially and temporally disaggregated extreme rainfall event.

2 Study area

Kathmandu valley is the upstream catchment of the Bagmati Basin, which extends between 85°11’ E to 85°31’ E longitude and 27°35’ N to 27°49’ N latitude in the Bagmati province in central Nepal (**Figure 1**). The catchment area of Kathmandu valley at Khokana, the focal area of this study, is approximately 654 km^2. The elevation of the catchment ranges from 1119 m to about 2714 m above mean sea level. The Bagmati River originates in the northern Shivapuri hills of Kathmandu and flows southwest until it is joined by the Manohara River flowing from the east (**Figure 1**). Then after travelling about 5.6 km in a westerly direction, the Bagmati River turns towards the south, where it is joined by another major tributary, the Bishnumati River, and it continues flowing south to where it leaves the Kathmandu valley. Other tributaries like the Hanumante, the Dhobi Khola, the Tukucha, the Balkhu, and the Nakhu rivers join the Bagmati along its path through Kathmandu. The Kathmandu Valley has a sub-tropical climate. The monthly average minimum temperature is about 3.4 °C while the monthly average maximum temperature is about 29.8°C (Lamichhane and Shakya, 2019). The precipitation regime is governed by the Indian Summer Monsoon (ISM), and the westerlies dominate the winter months (Nayava, 1980). The nature and behaviour of the summer monsoon and westerlies in Nepal are discussed by Kansakar et al. (2004) and Nayava (1980). The average annual precipitation is approximately 1660 mm with a standard deviation of 243 mm (computed from the observations from 1976 to 2016). Roughly 80 percent of the rainfall occurs during the monsoon months from June to September. Extreme events are related to the strength of the monsoon, and they commonly occur in the monsoon period, mostly in July and August (Pokharel and Hallett, 2015). The average annual flow of the Bagmati River at Khokana is approximately 16 m^3/s. In the monsoon months, the average flow is about 36 m^3/s, while in the winter months (December – February), the flow is only about 4.3 m^3/s. It reaches its lowest in April, with an average of only 3 m^3/s (computed from observations from 1992 - 2015). Based on the land-use and land-cover data of 2018, the agricultural land, forest and built-up area covered about 42%, 34% and 23% of the Kathmandu Valley, respectively (Lamichhane and Shakya, 2019). Historically, the highest recorded 24-hour rainfall at the catchment scale was about 178 mm in July 2002, which generated a peak flood discharge of approximately 942 m^3/s in the Bagmati River at Khokana.

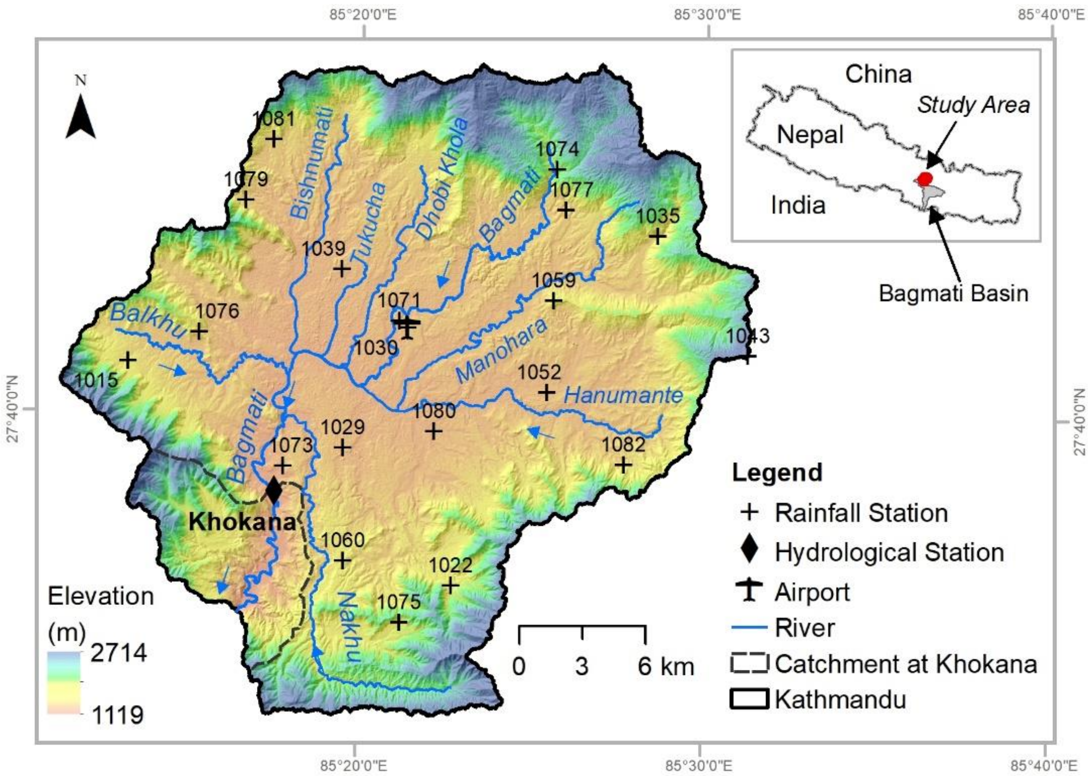

Figure 1: Topographic map of the Kathmandu Valley, including the river network and flow direction of the Bagmati River and its main tributaries, and the location of all rainfall stations in the region and the hydrological gauging station at Khokana to the south-west of the catchment. The location of the Kathmandu Valley within Nepal is shown in the top right insert.

3 Material and methods

The overall workflow followed in this study is presented in **Figure 2**. Components are described in the following sections.

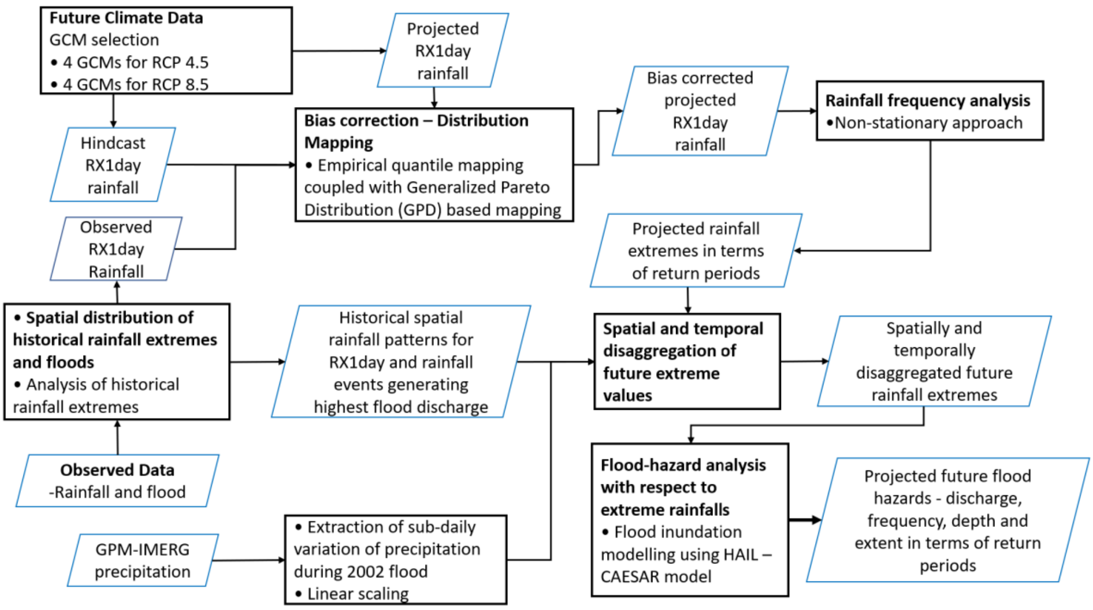

Figure 2: Flowchart with the methodology adopted in this study

3.1 Data collection and pre-processing

3.1.1 Observed data

Observed rainfall data from 23 stations and discharge data from the Khokana gauging station were collected from the Department of Hydrology and Meteorology (DHM), Nepal (**Figure 1**). Data quality was checked manually for missing data and any anomalies. 13 rainfall stations with data available for more than 20 years out of 30 years (1976 – 2005) were checked for homogeneity using the standard normal homogeneity test on annual precipitation. Only one station (index 1015) was found to be non-homogenous, with a possible detection of change in 1979. For this reason, the data from this station before 1979 was omitted. Data were checked manually for the remaining 10 stations, where data were available for less than 10 to 20 years and were found consistent. Missing rainfall data were filled using the inverse distance weighting method (IDW) spatial interpolation at a daily scale with a power factor of 2. Available records of sub-daily rainfall data are limited in length and inconsistent and, therefore, discarded in the rainfall analysis. Instantaneous maximum and daily mean discharge data at the Khokana gauging station were available from 1992 to 2015. Annual maximum instantaneous discharge at Khokana and corresponding 24-hour catchment rainfall in Kathmandu are presented in **Table 1**.

Global precipitation measurement (GPM) - Integrated Multi-satellitE Retrievals for GPM (IMERG) data -final rainfall estimate product (Huffman et al., 2019), with half hourly temporal resolution and 0.1° x 0.1° spatial resolution, were used in addition to the ground observation data for temporal disaggregation of the daily observed data. Available sub-daily discharge records for September 2021 have been used to calibrate the hydrodynamic model and the flood model was validated against the historical RX1day flood event in July 2002. Historical 25-year and 100-year return period floods were used as the base events for flood hazard modelling and were compared with future floods.

Table 1: Maximum instantaneous discharge at Khokana, corresponding catchment rainfall and RX1day maximum rainfall in Kathmandu

Year	Flood Date	Instantaneous Discharge (m^3/sec)	Catchment rainfall (mm)	RX1 day in 'mm' (Date of occurrence)
1992	20-07-1992	113.00	**38.90**	**39.1 (24-07-1992)**
1993	20-07-1993	938.00	**63.80**	**65.3 (22-07-1993)**
1994	07-08-1994	533.00	**56.70**	**69.3 (17-06-1994)**
1995	18-07-1995	393.00	**64.00**	**66 (13-06-1995)**
1996	14-07-1996	328.00	**64.80**	**64.8 (14-07-1996)**
1997	18-08-1997	493.00	**39.60**	**73.2 (01-07-1997)**
1998	09-07-1998	649.00	**71.80**	**71.8 (08-07-1998)**
1999	03-07-1999	421.00	**85.90**	**85.9 (03-07-1999)**
2000	08-08-2000	519.00	**67.20**	**67.2 (08-08-2000)**
2001	13-08-2001	275.00	**36.50**	**36.6 (20-07-2001)**
2002	22/23-07-2002	942.00	**178.30**	**178.3 (23-07-2002)**
2003	31-07-2003	421.00	**84.20**	**84.2 (31-07-2003)**
2004	09-07-2004	268.00	**79.10**	**79.1 (09-07-2004)**
2005	07-08-2005	226.00	**56.00**	**56 (07-08-2005)**
2006	19-07-2006	191.00	**35.70**	**37.2 (09-09-2006)**
2007	05-09-2007	424.00	**68.10**	**68.1 (05-09-2007)**
2008	03-08-2008	135.00	**35.50**	**35.5 (03-08-2008)**
2009	27-07-2009	375.00	**48.70**	**52.1 (28-07-2009)**
2010	07-09-2010	354.00	**52.70**	**52.7 (07-09-2010)**

2011	01-07-2011	480.00	**60.80**	**60.8 (01-07-2011)**
2012	03-08-2012	173.00	**39.20**	**39.4 (24-06-2012)**
2013	22-07-2013	130.00	**44.00**	**44 (22-07-2013)**
2014	14-08-2014	176.00	**41.10**	**47.1 (15-10-2014)**
2015	17-08-2015	364.00	**50.70**	**50.7 (17-08-2015)**

Note:
• Rainfall data recorded at collected at 8:00 am, which is accumulated value of last 24 hours. Flood gauge heights are collected at 8:00am, 12:00am and 4:00am. Therefore, flood data can have overlap of the rainfall from the given day and the previous day. So, catchment rainfall value represent maximum value in those days.
• Highlighted cells show that highest flow in given year is from RX1day rainfall.

3.1.2 Future climate data

Future rainfall projections were obtained from the Coupled Model Intercomparison Project 5 (CMIP5) General Circulation Models (GCMs) that are used in Nepal's National Adaptation Plan (MoFE, 2019). These GCM projections have been used previously in Nepal for vulnerability and risk assessment and for identifying the adaptation options in the water resources and energy sector (MoFE, 2021). It is to be noted that CMIP6 GCMs were still in the development phase, and limited CMIP6 GCMs were available when MoFE (2019) was prepared.

Nepal's National Adaptation Plan (NAP) considered CMIP5 GCMs in the spectrum of the projected temperature changes vs precipitation changes for each RCP 4.5 and RCP 8.5 scenario independently. MoFE (2019) considered a pool of 105 GCMs for RCP4.5 and 77 for RCP8.5 for the model selection. This pool has multiple ensemble members (variants) from each model. The selection of the GCMs in MoFE (2019), based on the approach by Lutz et al. (2016), followed three main steps:

The first step is the selection of 20 GCMs out of an available pool of CMIP5 GCMs based on their projections for changes in average temperature and precipitation for the future period of 2036-2065. The 10th and 90th percentile values of these changes were marked as the 'cold' and the 'warm' conditions for the projected temperature, and the 'dry' and 'wet' conditions for precipitation, respectively. The spectrum is divided into four conditions, namely cold-wet (CW), cold-dry (CD), warm-wet (WW) and warm-dry (WD). For instance, the warm-wet condition represents the 90th percentile of temperature change and the 90th percentile of precipitation change. Five GCMs were selected in each condition based on their proximity to those percentile values.

The second step is to filter 5 GCMs in each condition selected from the first step based on projected changes in extreme values of precipitation and temperature. MoFE (2019) used the Expert Team on Climate Change Detection and Indices (ETCCDI) indices R95pTOT (very wet days precipitation) and consecutive dry days (CDD) for precipitation, and the indices warm spell duration index (WSDI) and cold spell duration index (CSDI) for temperature. The two GCMs with the highest projected changes for those indices were selected in each condition.

The final step is the selection of one GCM for each condition based on the fidelity of the GCMs to represent the historical climate. MoFE (2019) accounted for the biases in monsoon, winter, and annual precipitation and temperature in GCMs compared to the observed precipitation and temperature for the historical period. Basing the selection of GCMs solely on changes in temperature and precipitation in the first step or on extreme indices in the second step may exclude GCMs with better performance in representing historical climate. Despite this limitation, for this study, we are relying on GCMs from MoFE (2019) to align with the national context of the NAP process. Please refer to MoFE (2019) and Lutz et al. (2016) for details on the model selection.

These steps were carried out for two possible trajectories (representative concentration pathway – RCP) of greenhouse gas concentration based on future emissions, namely RCP 4.5 and RCP 8.5 scenarios. RCP 4.5 scenario is the medium emission scenario, while RCP 8.5 represents the high emission scenario (van Vuuren et al., 2011). Selected GCMs are listed in **Table 2**. Projected changes were analysed for the three future periods; near-future (2016-2045), mid-future (2046-2075) and far-future (2076-2100). It is to be noted that the historical or baseline period is from 1976 to 2005. Historical runs for CMIP5 GCMs are up to 2005; therefore, we chose data up to 2005 as the baseline period. Data from the GCM grid cell corresponding to the location of Kathmandu were extracted using the nearest neighbour algorithm. Since we selected the models shown in **Table 2** from MoFE (2019), we didn't focus on the biases introduced by the choice of models selected or examine the sensitivity of the choice of ensemble members of the GCM model.

Table 2: Selected General Circulation Models (GCMs) based on the National Adaptation Plan for Nepal, MoFE (2019).

Conditions	Name of GCM
RCP 4.5 Scenario	
Cold-Wet (CW)	BCC-CSM1_1_r1i1p1
Cold-Dry (CD)	GFDL-ESM2M_r1i1p1
Warm-Wet (WW)	CanESM2_r2i1p1
Warm-Dry (WD)	MIROC-ESM-CHEM_r1i1p1
RCP 8.5 Scenario	
Cold-Wet (CW)	BCC-CSM1_1_r1i1p1
Cold-Dry (CD)	GFDL-ESM2M_r1i1p1
Warm-Wet (WW)	CanESM2_r5i1p1
Warm-Dry (WD)	MIROC-ESM-CHEM_r1i1p1

3.2 Precipitation-based extreme indices and 24-hour maximum rainfall

Attributes of the climatic extremes, such as frequency and magnitude, can be described with indices identified by the Expert Team on Climate Change Detection and Indices (ETCCDI) (Tank et al., 2009). These indices are widely used to study the global or local changes in future climatic extremes, like in Sillmann et al. (2013a, 2013b). In this study, a set of 9 precipitation related ETCCDI extreme indices, listed in **Table 3**, were analysed to quantify changes in future extreme precipitation for the Kathmandu valley.

Table 3: Precipitation extreme indices used in this study.

Name of Index	Description	Computational method
Annual maximum 1-day (or 24 hour) precipitation (RX1day) (mm)	Most intense rainfall event in 1 day (or 24 hours) for a given year	Let RR_{ij} be the daily precipitation amount on the day *i* in period *j*. Then maximum 1-day values for period *j* are $RX1day_j = \max(RR_{ij})$
Annual maximum consecutive 5-day Precipitation (RX5day) (mm)	Most intense rainfall event in 5 consecutive days for a given year	Let RR_{kj} be the precipitation amount for a 5-day interval ending *k* in period *j*. Then maximum 5-day values for period *j* are $RX5day_j = \max(RR_{kj})$
Heavy rainfall days (R10mm) (days)	Annual count of days when precipitation > 10 mm	Let RR_{ij} be the daily precipitation amount on the day *i* in period *j*. Count the number of days where $RR_{ij} > 10$mm
Very heavy rainfall days (R20mm) (days)	Annual count of days when precipitation > 20 mm	Let RR_{ij} be the daily precipitation amount on day *i* in period *j*. Count the number of days where $RR_{ij} > 20$mm

Consecutive dry days (CDD) (days)	Maximum number of consecutive days with daily precipitation (RR) less than 1 mm	Let RR_{ij} be the daily precipitation amount on day i in period j. Count the largest number of consecutive days where $RR_{ij} < 1$mm
Consecutive wet days (CWD) (days)	Maximum number of consecutive days with daily precipitation ≥ 1 mm	Let RR_{ij} be the daily precipitation amount on day i in period j. Count the largest number of consecutive days where $RR_{ij} \geq 1$mm
Very wet day precipitation (R95pToT) (mm)	Annual total precipitation when RR > 95 percentile of reference period	Let RR_{wj} be the daily precipitation amount on a wet day w (RR ≥ 1.0 mm) in period j and let $RR_{wn}95$ be the 95th percentile of precipitation on wet days in the reference period. If W represents the number of wet days in the period, then $R95pToT_j = \sum_{w=1}^{W} RR_{wj}$ where $RR_{wj} > RR_{wn}95$
Annual total wet day precipitation (PRCPTOT) (mm)	Total wet-day precipitation	Let RR_{ij} be the daily precipitation amount on the day i in period j. If I represents the number of days in j, then $PRCPTOT_j = \sum_{i=1}^{I} RR_{ij}$
Simple precipitation intensity index (SDII) (mm / day)	Simple daily intensity	Let RR_{wj} be the daily precipitation amount on wet days, RR > = 1 mm in period j. If W represents number of wet days in j, then: $SDII_j = (\sum_{w=1}^{W} RR_{wj})/W$

These indices represent different climate conditions that influence catchment runoff in terms of water availability and extreme events. The 24-hour maximum rainfall (RX1day) and or the 5-day maximum rainfall event (RX5day) represent climate conditions that can trigger floods and landslides (Pandey et al., 2021). Highly wet conditions are also indicated by very wet day precipitation (R95pToT). Consecutive high days (CDD) are linked to dry spells of low water availability or droughts. On the other hand, consecutive wet days (CWD) refer to increased wet conditions. Intense rainfall days (R10mm and R20mm) are related to the frequency of the rainfall and thus can cause high flows in the catchment. We note here that within Kathmandu, floods are triggered by rainfall events. In this study, 24-hour maximum rainfall (RX1day) was assessed to have a direct relationship with flood events (**Table 1**). Basnyat et al. (2020) showed a linear relationship between the RX1day rainfall and flood discharge at Pandherodovan in the Bagmati catchment, while Pandey et al. (2021) also showed a strong link between RX1day and high flows in a similar rainfed catchment in Nepal, the East Rapti.

3.3 Spatial distribution of historical rainfall extremes and floods

The spatial distribution of extreme rainfall is important as it affects local flood hydrographs and inundation (Wilson et al., 1979; Zoccatelli et al., 2011). Observed daily rainfall values were interpolated using inverse distance weighting (IDW) with a power parameter of 2 over a 1 km x 1 km grid of Kathmandu. To investigate the spatial distribution of rainfall, we selected rainfall events for the ten highest 24-hour maximum rainfall events (RX1day) in the historic record and the three events that generated the highest discharge at the Khokana gauging station. We normalised the rainfall values across the IDW interpolated grid to present them on a scale of 0 to 1 to compare spatial rainfall patterns across different events. The rainfall patterns were then analysed to identify the area of rainfall maxima during the event and the rainfall gradients across the catchment. The rainfall value was normalised by dividing its difference by the minimum value across the grid cells by the difference between the maximum and the minimum values across the grid cells.

3.4 Bias correction – Distribution Mapping

Biases in rainfall magnitude in GCMs during the historical period observation were corrected using the empirical quantile mapping method, a technique of mapping the probability distribution of rainfall of GCMs with the probability distribution of the observed rainfall. Details of this procedure are described in Gudmundsson et al. (2012). The procedure is given by the following relationship:

$$X^{corr}_{future,t} = inverse\ ecdf\ {}^{obs}_{reference}\left(ecdf^{Model}_{reference}\left(X^{Model}_{future,t}\right)\right),$$

where *ecdf* is the empirical cumulative distribution function (CDF) for the reference time period, $X^{Model}_{future,t}$ is the raw GCM at time *t* in the future, $ecdf^{Model}_{reference}$ is the empirical cumulative distribution function of the GCM for the reference period, and $inverse\ ecdf\ {}^{obs}_{reference}$ is the inverse empirical cumulative distribution function of the observed rainfall for the reference period. $X^{corr}_{future,t}$ is the corrected estimate of $X^{RModel}_{future,t}$. The relationship can be explained with **Figure 3 (A),** which shows *ecdf* for the model and the observation of the historical period. For any given future projection, $X^{Model}_{future,t}$ in the *x*-axis, the probability is given by $ecdf^{Model}_{reference}$ (red curve). The bias-corrected value, $X^{corr}_{future,t}$ is the value on the *x*-axis corresponding to the same probability on the reference $ecdf\ {}^{obs}_{reference}$ black curve.

For this study, we used the complete dataset of observations and GCM hindcast for the reference period of 1976-2005 to create the empirical cumulative distribution function (*ecdf*), defined for each month. Another variant called quantile delta mapping (QDM) was implemented along with quantile mapping. Quantile delta mapping preserves model-projected relative changes in the quantiles (Cannon et al., 2015). Details on QDM are described in Cannon et al. (2015).

Distribution mapping using empirical relationships works well for the normal range of rainfall values. But for extreme values or future projected values beyond the range of the observed values in the baseline period, extrapolation techniques like linear scaling based on upper quantiles are used. These can cause inflation issues, which are discussed in Cannon et al. (2015) and Maraun (2013). To reduce this inflation, distribution mapping was done with the theoretical distribution rather than the empirical distribution for the extreme values. Generalized Pareto Distribution (GPD) is commonly used as a theoretical distribution to model extreme values above a high threshold (Coles, 2001; Tank et al., 2009). Firstly, we computed the 99th percentile values for both observation and hindcast GCM for the reference period of 1976-2005. Then, we selected data points greater than the 99th percentile value for observations and GCM hindcast. Note that these threshold values are different for observation and hindcast. We considered the whole reference period of 1976-2005 without monthly breakdown. We fitted the theoretical GPD using Maximum Likelihood Estimation (MLE) and derived GPD based CDF for each of the observation and GCM hindcast datasets for the reference period of 1976-2005. Lastly, using this, we performed quantile mapping for the projected GCM data greater than the 99th percentile value of the hindcast (reference period) dataset. GPD curves for RCP 8.5 scenario for the warm wet condition are shown in **Figure 3 (B).** Note that, on rare occasions, linear scaling was still needed to adjust the values even when GPD based mapping was used.

An additional correction known as the "frequency adaption" was needed if the frequency of dry days in the reference period GCM data was greater than the frequency of dry days in the observed data (Themeßl et al., 2012). In this study, corrections were made for the extra dry days to prevent the artificial introduction of wet biases if any dry day is mapped as a wet day. Only the fraction,

$$\Delta P_0 = \frac{ecdf^{Model}_{reference}(0) - ecdf^{obs}_{reference}(0)}{ecdf^{Model}_{reference}(0)},$$

of such dry-day cases with probability P_0 are corrected randomly by uniformly sampling a number between zero precipitation and the precipitation amount of $inverse\ ecdf^{obs}_{reference,t}(\ ecdf^{GCM}_{reference,t}(0))$.

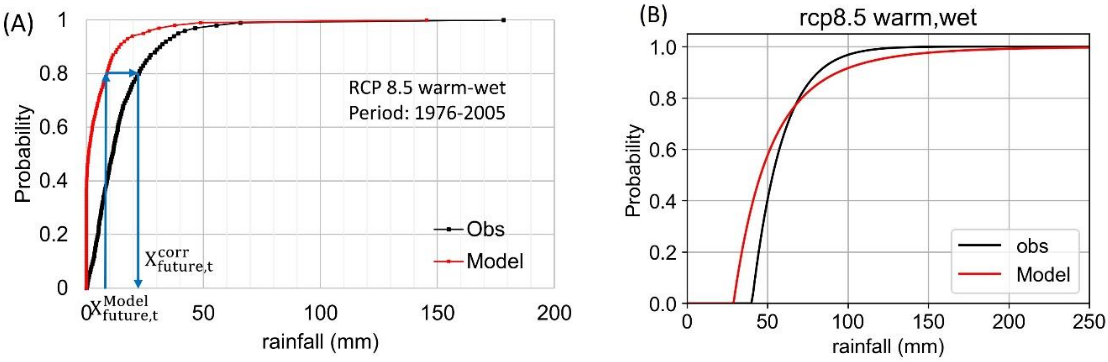

Figure 3: (A) Empirical cumulative distribution and (B) Generalized Pareto Distribution used for distribution mapping for RCP 8.5 warm wet condition.

3.5 Spatial and temporal disaggregation of future extreme values

Spatial disaggregation of the rainfall for the extreme values was based on the historical spatial distribution of rainfall events that generated the highest flood at Khokana. This rainfall pattern corresponded to the rainfall pattern on 22 July 2002 (**Figure 8**). In the formal DHM data record, the event is recorded as occurring on 23 July 2002 because the rainfall recorded at 8:45 am each morning refers to the accumulated rainfall of the preceding 24 hours. In the rainfall pattern of 22 July 2002, the rainfall maxima are located at the south and west of the Kathmandu valley (**Figure 8**), with over 160 mm of rainfall across most of the Kathmandu Valley catchment area.

Temporal disaggregation of the 24-hour rainfall was carried out using the temporal sub-daily pattern of the GPM IMERG product (Huffman et al., 2019). Temporal disaggregation of rainfall is essential because the catchment time of concentration at Khokana is approximately 6 hours based on estimations using Kirpich's equation (Kirpich, 1940). Therefore, daily rainfall is insufficient to model flood propagation through the catchment accurately. Automatic weather stations in the Kathmandu valley are sparse. They have only been installed in recent years, so it was not possible to adequately represent the sub-daily temporal resolution using observed data only. The temporal resolution of GPM IMERG was used to overcome this deficit because of its half-hourly resolution. Relative to the spacing of rainfall stations, the GPM IMERG spatial resolution, which is approximately 10 km x 10 km, is still low. However, the temporal rainfall pattern of GPM can be transferred to the station scale (from grid to station) using the following scaling approach.

Extreme rainfall values corresponding to different return periods were computed using non-stationary frequency analysis at the catchment scale, described in **Section 3.6**. Spatial and temporal disaggregation for a given return period event was achieved simultaneously in the following steps: (a) Observed rainfall on 22 July 2002 for each of the stations was first divided by the catchment average rainfall for the same date and multiplied by the rainfall value of the given return period. This approach linearly scales observed rainfall on 22 July 2002 to the rainfall value of the given return period. (b) GPM IMERG sub-daily precipitation was aggregated to a daily scale after extracting the rainfall values for each observation station using the nearest neighbour algorithm. (c) A scaling factor was computed as the ratio of observed rainfall values for each station to a daily GPM IMERG rainfall value. (d) The scaling factor was then multiplied by sub-daily GPM IMERG to obtain the scaled sub-daily precipitation corresponding to the given return period.

3.6 Rainfall frequency analysis

Stationary rainfall frequency analysis is conventionally used for quantifying the rainfall value associated with a given probability. For water resources development, this poses a challenge because the fundamental assumption of stationarity in the climate system is questionable when climate change is considered (Milly et al., 2008). As warming continues, precipitation extremes are observed to be on the rise globally, and future projections of GCMs predict an increase globally and in the South Asian region (Sillmann et al., 2013b). To incorporate these time-variant processes, the frequency analysis used non-stationary models that allow probability distribution functions (pdfs) of time-dependent and non-stationary extreme rainfall (Coles, 2001).

In this study, for non-stationary rainfall frequency, the approach described in Coles (2001) and Wi et al. (2016) was used. Non-stationary analysis has been recommended for climate change conditions by the Committee on Adaptation to a Changing Climate (2018). A Mann-Kendall trend test was carried out to test the time series trend. For the future data period of 2006-2100, a non-stationary process was adopted. For the historical observations from 1976-2005, the trend was not significant, and the stationary frequency analysis was deemed sufficient.

Generalized extreme value (GEV) distribution for the annual maximum series of RX1day rainfall was used in the study (block maxima approach) (Chow et al., 1988). GEV distribution is commonly used for non-stationary frequency analysis of annual maxima for rainfall, as in Wi et al. (2016) and Ragno et al. (2018). The GEV distribution function, as defined in Coles (2001), is given by:

$$G(z) = exp\left\{-\left[1 + \xi\left(\frac{z-\mu}{\sigma}\right)\right]^{-\frac{1}{\xi}}\right\}, \text{ .....Equation 1}$$

where μ, σ and ξ are location, scale and shape parameters, respectively. Here, the parameters satisfy $-\infty < \mu < \infty, \sigma > 0$ and $-\infty < \xi < \infty$. If $\xi \rightarrow 0$, it leads to Gumbel distribution which is given by:

$$G(z) = exp\left\{-exp\left[-\left(\frac{z-\mu}{\sigma}\right)\right]\right\}, \text{ ......Equation 2}$$

and the T- year return level value (X_T) for extreme rainfall is estimated as,

$$X_T = \mu + \frac{\sigma}{\xi}\left[1 - \left\{-log\left(1 - \frac{1}{T}\right)\right\}^{-\xi}\right], \text{ ......Equation 3}$$

The key assumption of GEV is that the extreme values are independent and identically distributed. Any presence of a trend violates this assumption (Wi et al., 2016). In this regard, the non-stationary case is introduced by considering the parameters of GEV as a function of time. Generally, the location and scale parameters are taken as a function of time (Committee on Adaptation to a Changing Climate, 2018; Wi et al., 2016). In this study, four cases were considered, shown in **Table 4**.

Table 4: Specification of parameters used in the generalized extreme value distribution (GEV).

Case	Description	Notation used
A	Location parameter is function of time for 2006-2100. Distribution is given by: $GEV\ (\mu(t), \sigma, \xi)$ $\mu(t) = \beta_0 + \beta_1 \times t$ where, $\beta_0\ and\ \beta_1$ are parameters.	NS-GEV-M1
B	Location and scale parameters are function of time for 2006-2100. Distribution is given by: $GEV\ (\mu(t), \sigma(t), \xi)$ $\mu(t) = \beta_0 + \beta_1 \times t$ $\sigma(t) = C_0 + C_1 \times t$	NS-GEV-M2

	where, β_0 *and* β_1 and C_0 *and* C_1 are parameters.	
C	Parameters are constant in time during 2006 – 2100	S-GEV
D	Parameters are constant in time during given time period (near future, mid future and far future)	S-GEV (near-future NF or mid-future MF or far-future FF)
Note: NS and S represent non-stationary and stationary approaches, respectively. GEV represent Generalized extreme value.		

In the RCP 8.5 warm-wet case, the non-stationary (NS) Gumbel distribution was used instead of NS GEV M1 because of issues related to the shape parameter, described in section 4 below. The parameters of stationary and non-stationary distributions for a given sample N (N = 30 for the historical period 1976-2005, and N = 95 for the future period 2006-2100) were estimated by the maximum likelihood estimation (MLE) approach as described in Coles (2001) and Wi et al. (2016). Location and shape parameters were estimated using MLE as a linear function of time in the non-stationary case, and the values of estimated parameters were compared considering changes in sample number and time frame. So, for the future period 2006-2100 (95 years), we used two approaches – one with the moving window where the number of samples is fixed (N = 30) and the other with the incremental window (where the number of samples increases, starting from N= 30 to N=95, as we move into the future by one year at a time). The advantage of using the MLE method is that it allows estimation of the confidence intervals of the distribution quantiles. This is possible due to the asymptotic normality of the ML parameter estimator; the maximum likelihood estimator will have an approximately normal distribution as the sample size gets sufficiently large (Wi et al., 2016). Parameters were estimated using the R programming environment with the *ismev* library (Stephenson et al., 2018).

3.7 Flood-hazard analysis under extreme rainfall

To explore flood propagation through the Kathmandu Valley for different historical and future scenarios, the rainfall time series were used as input in the numerical model HAIL-CAESAR (Valters, 2017). The HAIL-CAESAR model is an open-source, high-performance, parallelised C++ implementation of the Caesar-Lisflood algorithm (Coulthard et al., 2013). It combines the cellular automation landscape evolution model, Caesar (Coulthard et al., 2002), with the hydrological flow model, Lisflood (Bates et al., 2010). For this rainfall-driven flood analysis, the landscape evolution component of Hail-Caesar was disabled. The Lisflood algorithm has been used widely in small and large-scale flood analysis, including as part of a European-wide flood analysis project (Dottori et al., 2022; Feeney et al., 2020; Malgwi et al., 2021). Although Lisflood uses a simplified version of the shallow water equations for flow routing, it has been shown to yield results within 10% accuracy of full shallow water models while allowing for significant gains in computational time (Neal et al., 2012).

All simulations presented in this study were run using a 10 m Digital Elevation Model (DEM), resampled from a 2 m resolution DEM derived from tri-stereo Pleiades satellite imagery captured in 2019. The model mesh size is the same as the DEM cell size. A detailed description of the numerical model and flow routing algorithms can be found in Bates et al. (2010) and Coulthard et al. (2013). A spatially varied rainfall time series is applied to each cell in the model domain using the Thiessen polygon method (Herschy et al., 1998; Thiessen, 1911). Rainfall runoff is generated using an adaptation of the TOPMODEL (Beven and Kirkby, 1979) and the parameter *m*, which determines the runoff rate. Because of the large size of the catchment and the lack of high resolution land-use maps, this study used a uniform Manning's coefficient for the whole catchment. The Manning's coefficient, *n* and the TOPMODEL *m* parameters were calibrated for the September 6th 2021, flood event (Error! Reference source not found.). This flood event had a maximum local precipitation of 116 mm in 24 hours, recorded in the northern part of the catchment (Sankhu), and a 24-hour catchment average rainfall of

56 mm (Error! Reference source not found.). The model performance was evaluated by analyzing the hydrograph patterns and statistical measures such as Nash-Sutcliffe efficiency (NSE) and the coefficient of determination (R^2). The values of m and n that gave the best results in the calibration test were 0.003 and 0.03 $m^{1/3}s^{-1}$, respectively (**Figure 4** and **Figure 5**). The small m value represents a flash flood event, where most rainfall contributes to surface runoff.

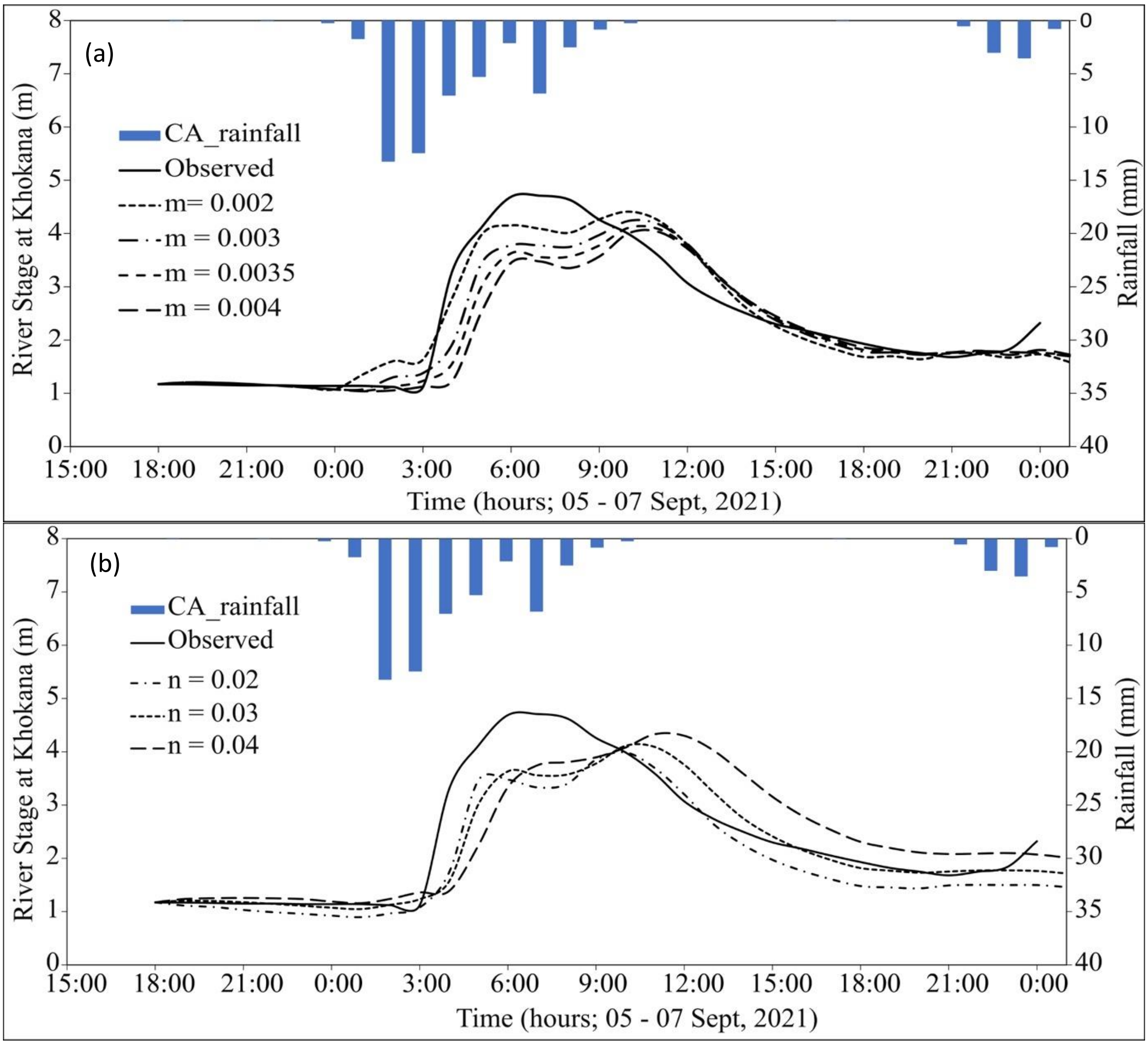

Figure 4: Comparison of observed (solid black line) and simulated (dashed lines) stage height (m) at Khokana gauging station, close to the outlet of the catchment (location shown in Figure 1); (a) shows simulated stage for model runs with constant Manning's coefficient, n = 0.04 $m^{1/3}s^{-1}$, and variable TOPMODEL m parameter from 0.002 to 0.004; (b) shows simulated stage height for simulations with constant m = 0.003, and variable Manning's coefficient, n.

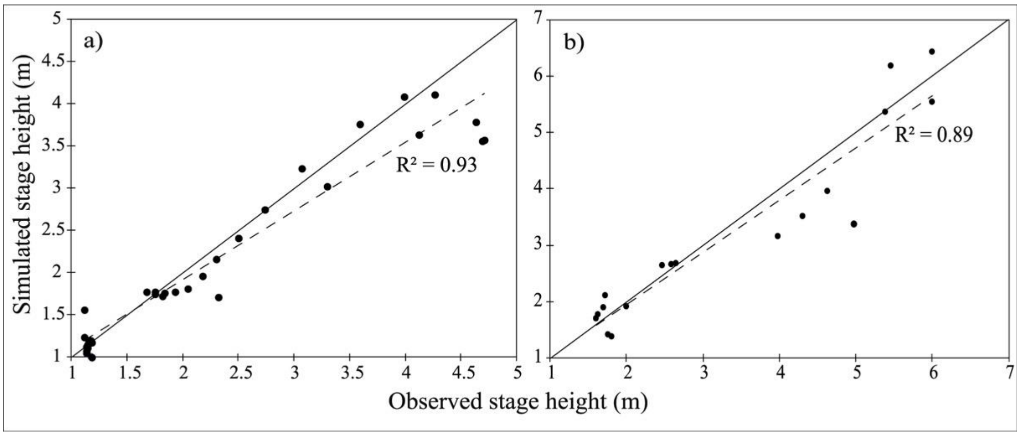

Figure 5: Scatter plot diagram showing observed versus simulated height for Bagmati River at Khokana during a) calibration test (September 2021 event) and b) validation test (July 2002 event). R^2 trend line given as dashed line.

Figure 6 presents results for the observed and simulated stage height at the Khokana gauging station, which is close to the outlet of the Kathmandu catchment, for the calibration (6 a) and validation (6 b) tests, for optimum *m* and *n* values. For the calibration test, in the numerical model, the arrival of the flood wave is delayed by approximately 1 hour, but the peak stage magnitude and shape of the flood wave are comparable. We note that the simulated hydrograph displays two peaks, following the two peaks in rainfall intensity, but the observed hydrograph shows a single flood peak. This is likely related to the use of rainfall data that was only available for 9 out of 17 stations across the catchment and thus may not be representative of the actual rainfall which occurred during the event. The model was then validated for the peak historic flood, the event that occurred on July 22nd, 2002, using rainfall data from 17 gauging stations. As seen in Figure 6b, there is good agreement between the observed and simulated stage heights, although it is possible that the simulated results underestimate the peak flood which likely occurred between 16:00 on 22/07/2002 and 08:00 on 23/07/2002 but was not captured by the recorded data.

Following successful validation and calibration, values of m = 0.003 and n = 0.03 $m^{1/3}s^{-1}$ were selected for all further flood model simulations in this study.

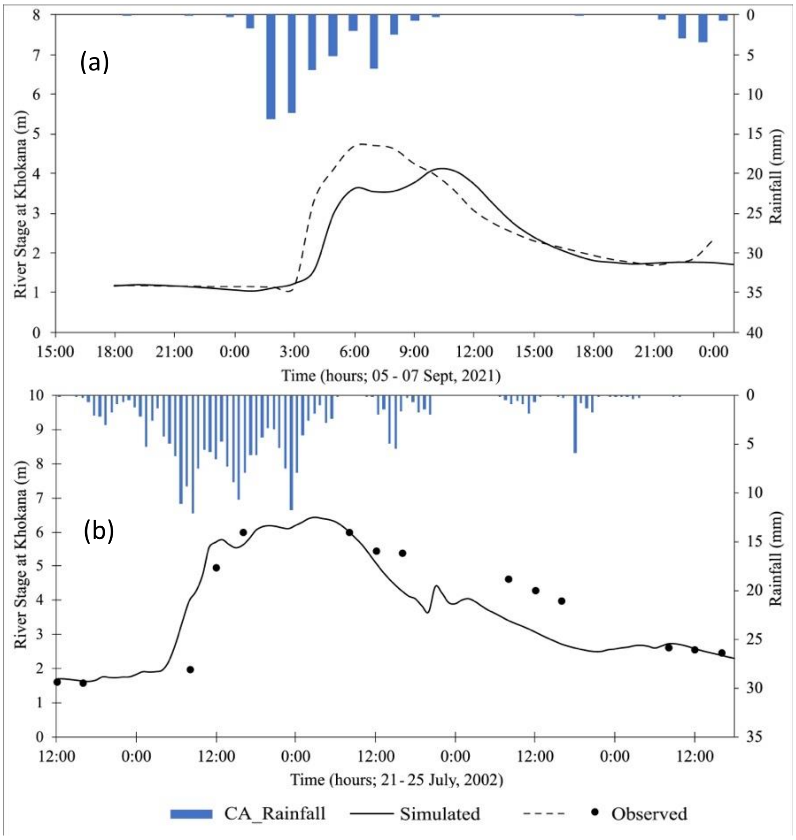

Figure 6: Comparison of simulated and observed stage height (m) at the Khokana gauging station for (a) the calibration test flood event on 6th September 2021, and (b) the validation test against the flood on 22nd July 2002. In both cases the TOPMODEL *m* = 0.003, and Manning's coefficient, *n* = 0.03 $m^{1/3}s^{-1}$. Hourly catchment average rainfall (mm) is shown as blue histogram bars.

4 Results and discussion

4.1 Relationship between spatio-temporal distribution of rainfall in Kathmandu and floods

The spatial distribution of rainfall across the Himalayas is strongly influenced by topography (Bookhagen and Burbank, 2006); this is also the case in the Kathmandu valley. The central valley floor receives about 1500 mm of annual average rainfall, while the hill slopes receive up to 2400 mm of rainfall, and, in general, rainfall is concentrated over the northern hills. The annual precipitation distribution is shown in **Figure 7**. Spatial heterogeneity of rainfall in Kathmandu occurs due to the interaction between the monsoon wind and the surrounding hills in Kathmandu. In the monsoon, the flow of moisture-laden wind enters the valley mainly from the west, southwest and south directions (Aryal et al., 2008). As it passes the southern hill ridge, rainfall occurs over the southwest flank of the valley. Once the wind encounters the hills in the north, further orographic enhancement of precipitation occurs (Anders et al., 2006; Roe, 2005). Intense precipitation can be highly localised when convective storms are influenced by Himalayan topography (Hobley et al., 2012). Besides, precipitation extremes during the monsoon season are attributed to the synoptic conditions of low-pressure systems, mid-level troughs, western disturbances and break monsoon conditions, as described in Bohlinger et al. (2017) and Richardson (2021). In Kathmandu, low intensity rainfall ranging from 0.01 mm/hr to 0.25 mm/hr contributes a larger percentage of the total precipitation than higher intensity rainfall ranging from 4.25 mm/hr to 4.50 mm/hr (Pokharel and Hallett, 2015). However, higher intensity rainfall is the primary driver of floods.

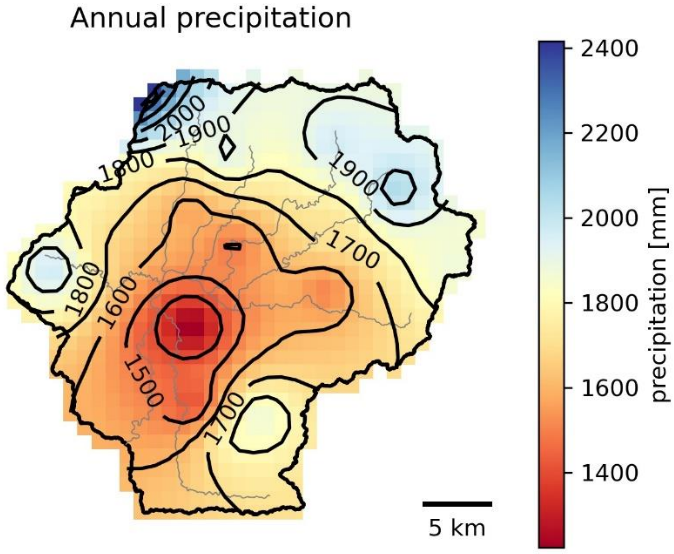

Figure 7: Annual rainfall in Kathmandu

The spatial pattern of extreme rainfall differs from the annual rainfall pattern in terms of the location of maxima. For extreme rainfall events, the rainfall maxima are concentrated in the west and southwest regions of the valley (**Figure 8**) because the moisture-laden wind enters from this direction. In contrast, annual rainfall is concentrated over the northern region (**Figure 7**). This demonstrates the difference between high and low intensity rainfall patterns in the region. **Figure 8** (A) illustrates the spatial distribution of the top 5 highest RX1day (catchment average) rainfall events, and (B) shows rainfall patterns that generated the highest floods recorded at the Khokana gauging station. In both (A) and (B), the top row shows the actual rainfall, while the bottom row shows the normalised rainfall at a scale of 0 to 1. Cross-sectional profiles of extreme rainfall events (**Figure 9**), further illustrate that higher rainfall intensity occurs in the southwest region compared to the northeast region. Similar patterns are observed for extreme rainfall distribution that causes floods at Khokana.

The spatial distribution and magnitude of rainfall events that generated floods at Khokana (**Figure 8** B) are different from the RX1day events (**Figure 8** A), although all conditions presented in **Figure 8** are wet enough to produce high flows. This is due to the difference in travel time of rainfall runoff to Khokana. We estimated the travel time using Kirpich's equation (Kirpich, 1940). The approximate travel time from the northern hills (Sundarijal, the origin of the Bagmati River) to Khokana is estimated to be approximately 11 hours, while from the southern hills (near the origin of the Nakku tributary), it is estimated to be about 6 hours. If we consider flood hazards in other areas of the Kathmandu Valley, the spatial distribution of extreme rainfall becomes even more important in the analysis because of different times of concentration of the peak flood.

In **Figure 8**, the spatial patterns of 1978, 1994 and 2000 events are different to the seven rainfall events. These rainfall patterns, where the highest rainfall occurred in the northern hills, could have had a higher impact in the areas of the north of Kathmandu compared to Khokana because the severity of flooding at different locations depends on the rate at which rainfall accumulates, the spatio-temporal pattern of rainfall, and the travel time. Among all the patterns shown in **Figure 8**, the spatial pattern of rainfall that produced the highest flow at Khokana is also the highest RX1day event, so we chose this pattern for spatial disaggregation of future rainfall events. For the purpose of this study, we do not examine the sensitivity of future rainfall events to varying spatial patterns.

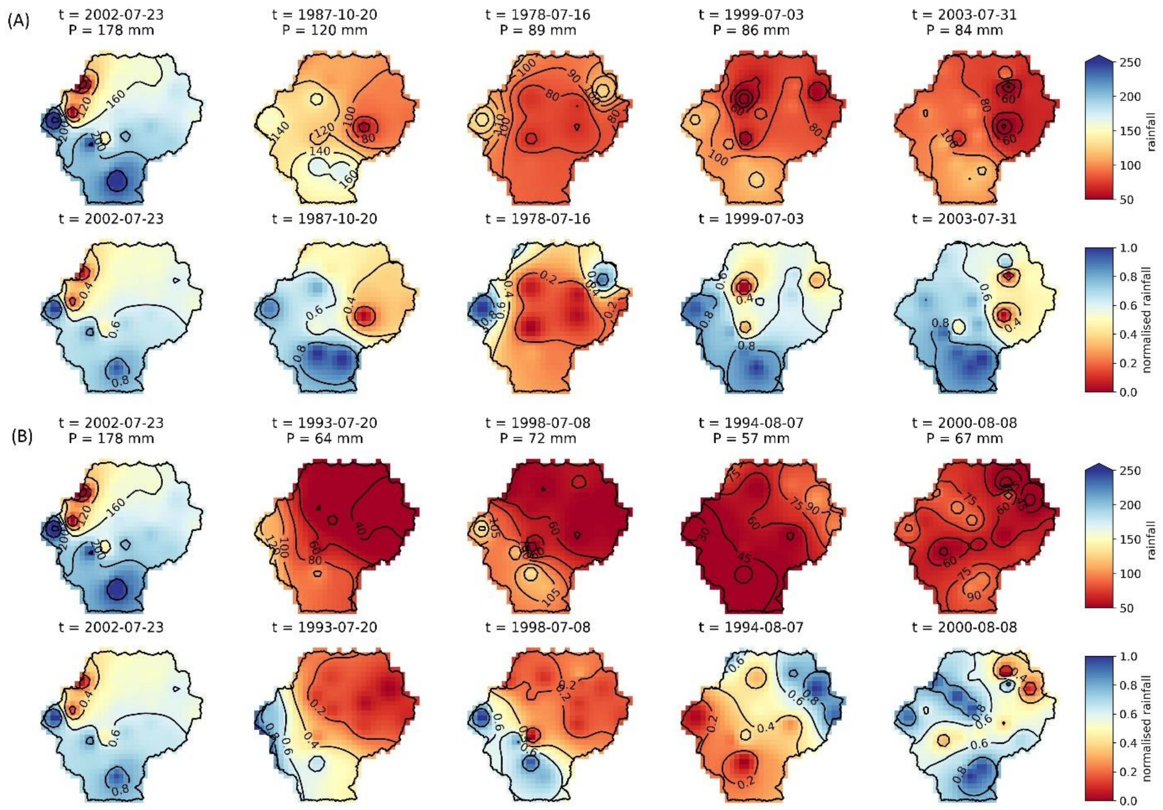

Figure 8: Spatial pattern of extreme rainfalls in Kathmandu for (A) top five RX1day rainfall and (B) rainfall events that generated the top five highest floods at Khokana station. Top row indicates the magnitude of rainfall in millimetres, while bottom row shows normalised rainfall.

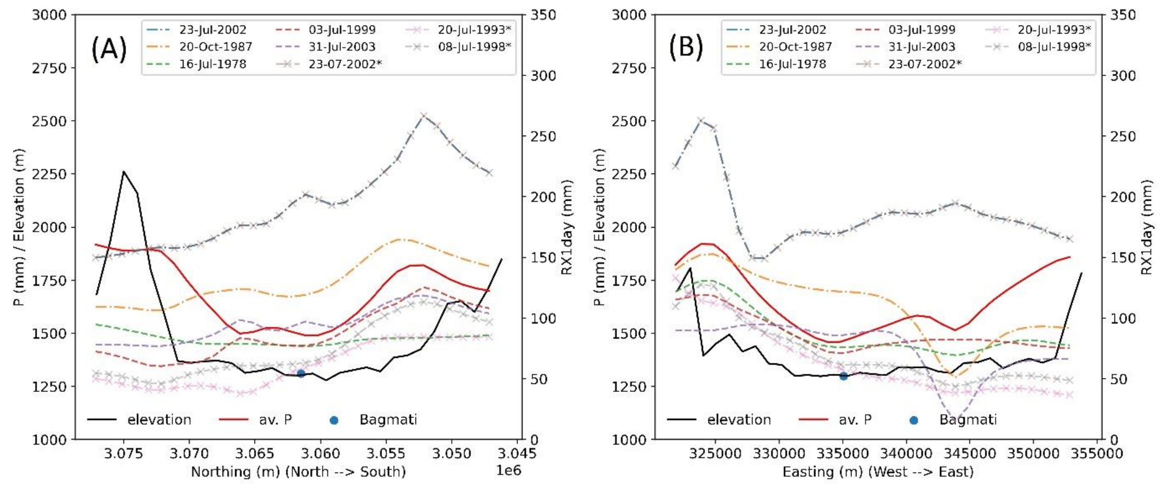

Figure 9: Cross section of elevation and rainfall in the Kathmandu Valley (A) North-South Direction (B) West–East direction

Results of the temporal disaggregation of the 2002 RX1day event show that rainfall was particularly heavy on 22 July 2002 from 00:00 to 12:00, with some stations exceeding 20 mm of rain in an hour (**Figure 10** A). This incessant rainfall caused the peak discharge of 942m³/s at Khokana. The south and west regions of Kathmandu received higher rainfall than the northern regions during this event. The daily GPM IMERG precipitation data bears a good correlation (R = 0.96) with the gauged observations at the daily scale (**Figure 10** B). In the study, the performance of the temporal distribution of the GPM-

IMERG product at a sub-daily scale over Kathmandu or Nepal as a whole has not been evaluated. Since hourly rainfall data for the Kathmandu valley is scarce, lacks consistency, and is of questionable quality whenever available, it was not used for the study. Despite the uncertainty associated with the sub-daily temporal distribution of GPM-IMERG rainfall over Kathmandu, previous studies have shown good performance of GPM-IMERG products at a daily scale in capturing the patterns of spatial precipitation extremes in Nepal. Nepal et al. (2021), Sharma et al. (2020) and Talchabhadel et al. (2022) showed that GPM-IMERG can capture the spatial variability and patterns of precipitation indices over Nepal, with the constraint that it underestimates the precipitation magnitude. **Figure 10 B** also shows that the GPM-IMERG product underestimates rainfall in Kathmandu. A linear scaling was performed to remove the biases in the estimate of total daily precipitation. However, because the scaling is linear and applied at the catchment scale, the sub-daily temporal distribution and spatial distribution pattern remain unchanged. Since the time resolution of the GPM IMERG product is 30 minutes, it is useful to model the flood response to the rainfall because of the short time of concentration to Khokana.

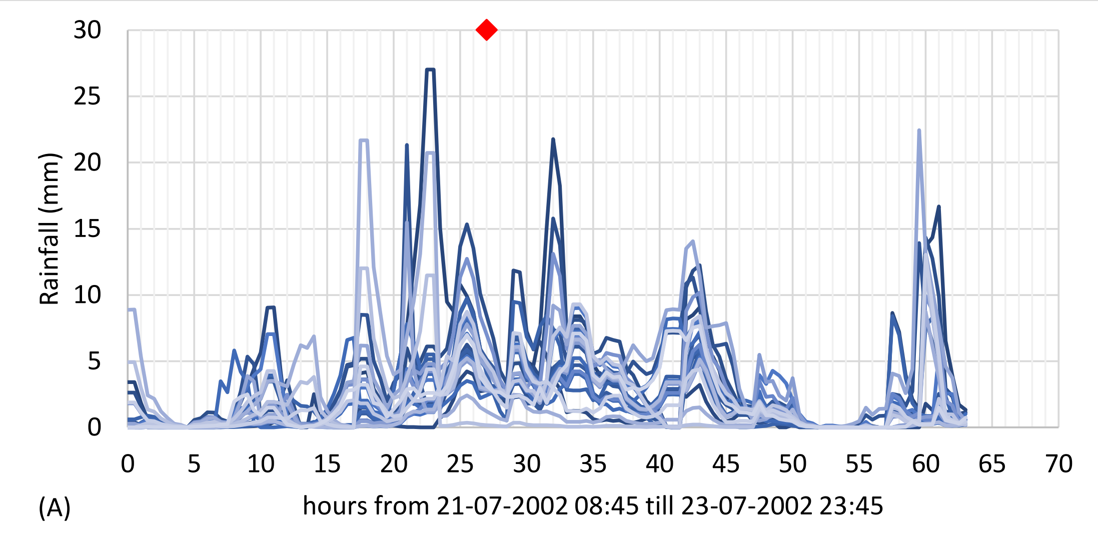

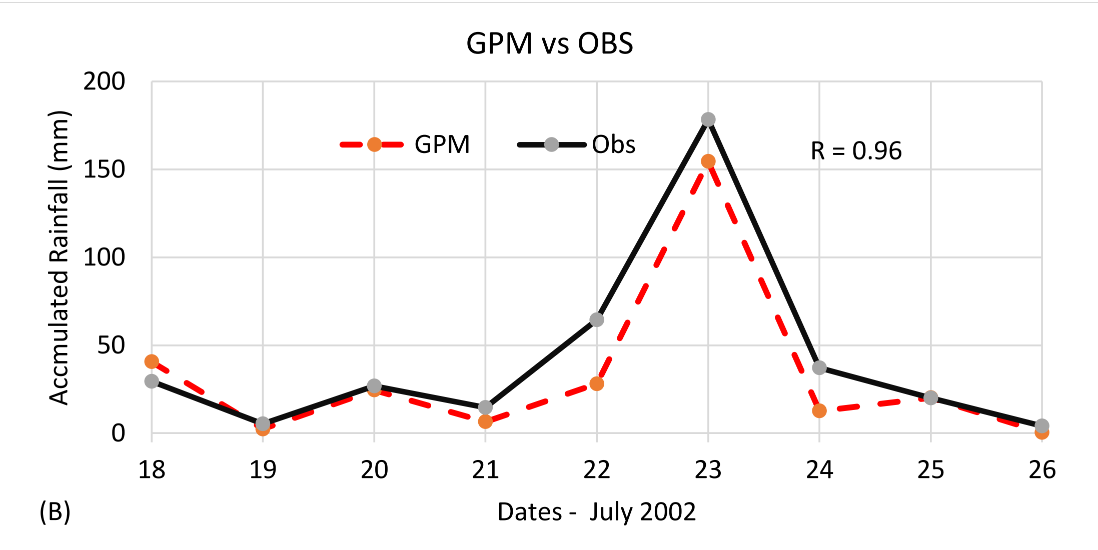

Figure 10: GPM precipitation (A) temporal variation of GPM precipitation at 23 stations (shown in Figure 1) for 22 July 2002 event and red star shows instantaneous flood peak of magnitude 942 m^3/sec (B) Comparison of daily GPM rainfall and observation at catchment scale

4.2 Bias correction of GCMs

Long-term monthly observed precipitation and hindcast GCM precipitation for the reference period 1976-2005 are shown in **Figure 11** A. The selected GCMs, listed in **Table 2**, show reasonable reliability to represent the seasonal cycle of the summer South Asian Monsoon. Even though step three in the GCM selection method aims to ensure minimal bias in the monsoon and winter precipitation and temperature, some biases were still present. Performance of the empirical quantile mapping (QM) and quantile delta mapping (QDM) using a split-sample cross-validation approach for the period of 1976-2005 were found to reduce biases. This can be observed in **Figure 11** B and C. **Figure 11** B shows an example of monthly precipitation for the CanESM2_r5i1p1 model, selected for the warm-wet condition in the RCP 8.5 scenario before and after bias correction. **Figure 11** C compares the biases in the model before and after bias correction using quantile mapping and quantile delta mapping. Raw GCM show negative biases more than 50% for the monsoon months. In this case, the quantile delta mapping reintroduced positive biases of about 90% in the months of January and February, and this is due to the higher number of dry days in those months. Quantile delta mapping over-fits long-term average values in the monsoon. Quantile delta mapping, by design, is not meant to adjust the mean values; instead, it adjusts the biases in the quantiles (Cannon et al., 2015).

Performance of QM and QDM coupled with Generalised Pareto Distribution (GPD) based distribution mapping were also evaluated to account for inflation in the future period. QM and QDM tend to exaggerate the projected values due to scale mismatch when downscaling from grid box level to the local scale (Cannon et al., 2015; Maraun, 2013); when projected values are beyond the range of historical values (which the cumulative distribution function is derived from), linear scaling based on the ratio of higher quantile values or other techniques like regression are applied. Thus, QM and QDM approaches (without GPD) were inflating the projected RX1day values compared to the raw GCM RX1day values. **Figure 12** presents results for RX1day rainfall after quantile mapping. In **Figure 12** A, as a result of the linear scaling, an ensemble member for the RCP 8.5 scenario (light red line), bias-corrected using quantile mapping, repeatedly estimated more than 300 mm of precipitation (400mm in some cases). **Figure 12** B shows how the inflation of projected RX1day values is reduced for the RCP 8.5 scenario (light red line) when quantile mapping is coupled with Generalized Pareto Distribution (GPD) based mapping. Comparison of projected changes in RX1day rainfall before and after bias correction with QM, QDM, QM coupled with GPD, and DQM coupled with GPD are shown in **Table 5.** For instance, in the near future, for the RCP 8.5 scenario, the changes in RX1day rainfall average (ensemble mean of four GCM models for RCP 8.5 scenario) for uncorrected GCM is 15% in contrast to 37% and 41% (**Table 5**) by quantile mapping and quantile delta mapping, respectively. When correction was done using quantile mapping and quantile delta mapping followed by GPD, these values reduced to 6% and 14%, respectively (**Table 5**). The differences in values between these different approaches to bias correction demonstrate the uncertainty of bias correction processes.

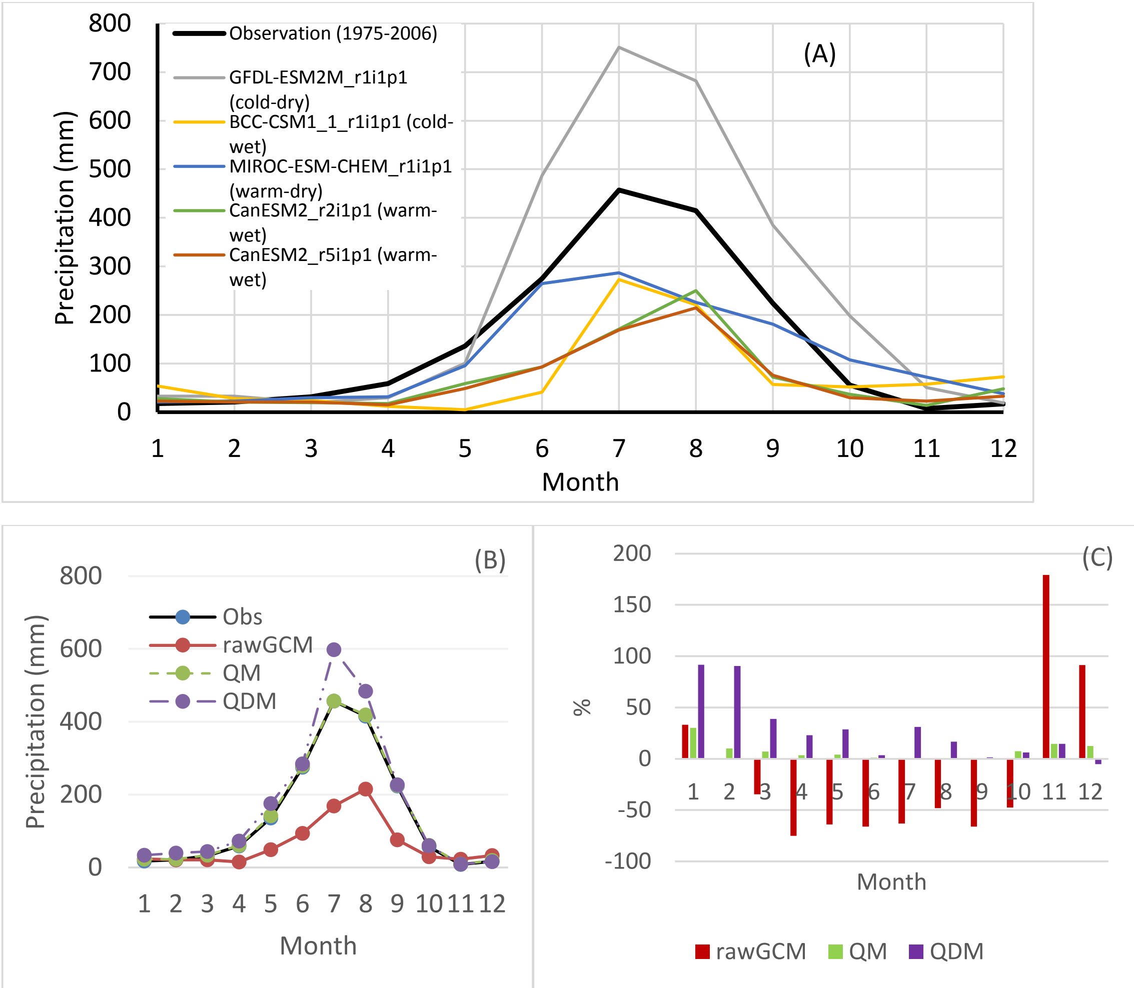

Figure 11: (A) Long-term monthly precipitation for reference period 1976-2005 (B) Long-term monthly precipitation of CanESM2_r5i1p1 model (warm-wet condition) for reference period 1976-2005 before and after bias correction in validation process against the observation (C) Monthly biases (in percentage) in precipitation for CanESM2_r5i1p1 model (warm-wet condition) for uncorrected model and after quantile mapping (QM) and quantile delta mapping (QDM) for reference period 1976-2005

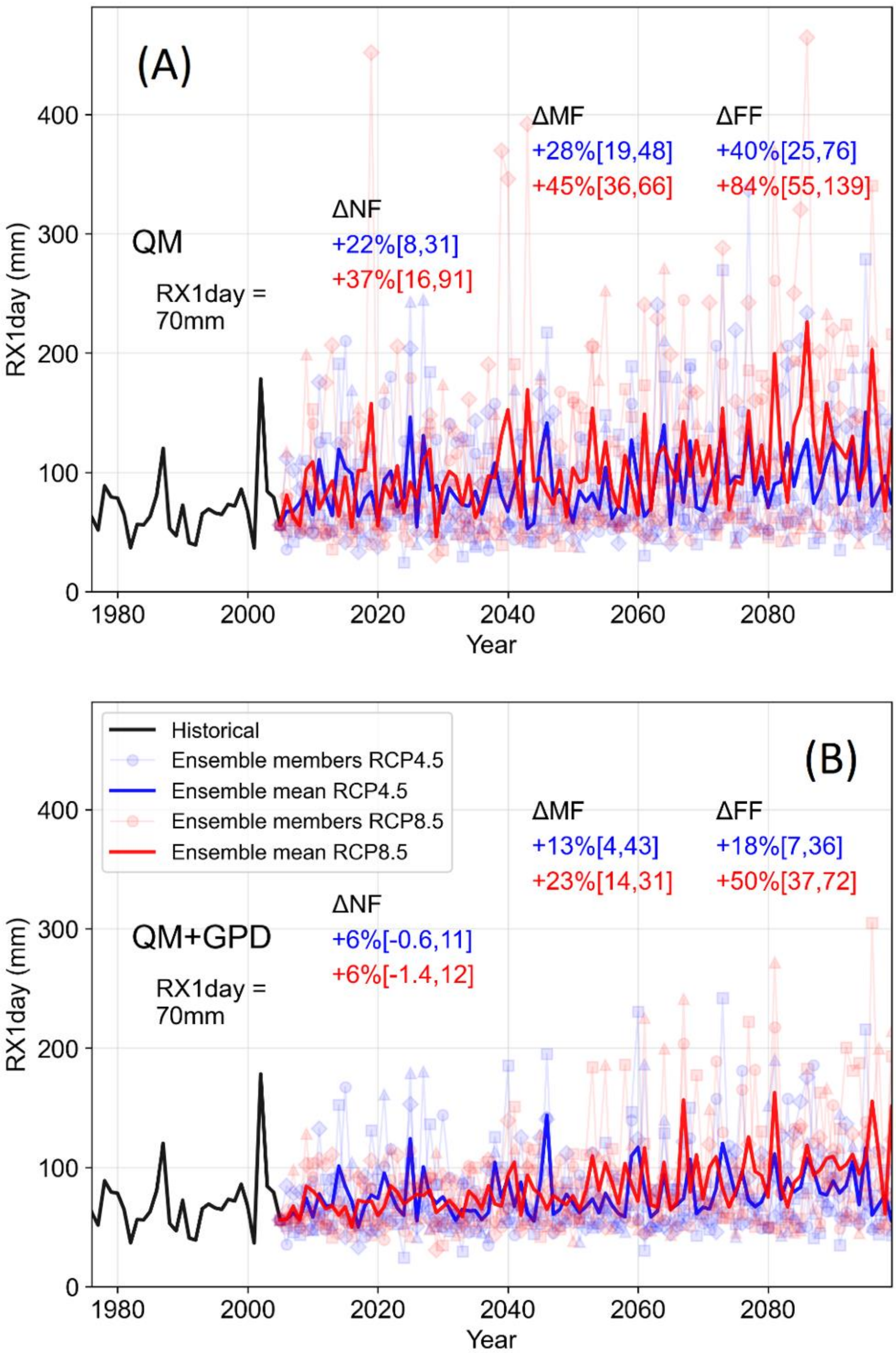

Figure 12: (A) RX1day rainfall after quantile mapping (QM); (B) RX1day rainfall after quantile mapping followed by GPD based distribution mapping. Rainfall projections shown for near future (NF), mid future (MF), and far future (FF) for RCP4.5 and RCP 8.5 scenarios. (Note: Only quantile mapping results are shown in the figure)

Table 5: Projected changes in average RX1day precipitation in near (NF), mid (MF), and far (FF) future using different approaches of bias correction: quantile mapping (QM), quantile delta mapping (QDM) and Generalised Pareto Distribution (GPD)

`		Changes in RX1day (%)														
Scenarios	Observed average RX1day (mm)	Uncorrected			Bias Corrected QM			Bias Corrected QDM			Bias Corrected QDM + GPD			Bias Corrected: QM + GPD		
		NF	MF	FF	NF	MF	FF	NF	MF	FF	NF	MF	FF	NF	MF	FF
rcp4.5 cold-dry		8	9	11	31	19	31	17	16	22	9	12	17	8	9	14
rcp4.5 cold-wet		6	27	9	8	48	27	15	37	21	20	40	13	6	33	7
rcp4.5 warm-dry		13	8	18	30	15	25	16	14	19	11	5	16	11	4	16
rcp4.5 warm-wet		16	25	71	18	32	76	21	40	78	4	10	39	-1	5	36
Average	70	**11**	**17**	**27**	**22**	**28**	**40**	**17**	**27**	**35**	**11**	**17**	**22**	**6**	**13**	**18**
rcp8.5 cold-dry		3	17	28	16	36	55	4	21	39	0	18	39	-1	18	37
rcp8.5 cold-wet		9	29	47	18	40	85	38	47	75	36	50	92	4	31	72
rcp8.5 warm-dry		12	25	39	21	38	56	16	33	43	7	29	43	7	29	43
rcp8.5 warm-wet		36	33	114	91	66	139	105	76	137	14	15	47	12	14	46
Average		**15**	**26**	**57**	**37**	**45**	**84**	**41**	**44**	**73**	**14**	**28**	**55**	**6**	**23**	**50**

4.3 Projected changes in future precipitation and precipitation extreme indices

Our analysis shows that precipitation is projected to increase in the future for Kathmandu. All GCMs project an increase in mid-future and far-future precipitation within a range of 3 to 37%, with an ensemble mean of 9% in the far future for the RCP 4.5 scenario, and 21% for the RCP 8.5 scenario. The near future GCMs for warm conditions show a slight decrease in rainfall for RCP 4.5 scenario. In the RCP 8.5 scenario, precipitation is projected to decrease slightly in the near future, warm-dry condition. For the wet future scenario, similar projections for other Nepalese river basins have been presented in various past studies such as Kaini et al. (2021); Pandey et al. (2020); Talchabhadel and Karki (2019).

Precipitation extreme indices in the Kathmandu Valley are also projected to increase in the future. Future projections for the RX1day precipitation (maximum 24-hour rainfall) are shown in **Figure 12** and **Table 5**. The long-term historical average (from 1976-2005) RX1day value is 70mm which is projected to increase. Changes in RX1day range from a slight decrease (-1%) to an increase of 72% in the combined QM and GPD approach (**Table 5**). The decrease in RX1day for the near-future under the RCP 4.5 scenario is due to the effect of the bias-correction procedure described in Section 4.2. The limitation of the quantile mapping approach is that trends are not preserved; therefore, the values of the bias-corrected variable (as well as the changes compared to the historical data) may be different from those obtained without bias correction. When QM is coupled with GPD, changes in RX1day precipitation are about 6% [-1% to 12%] (**Table 5**) in the near future for both RCP scenarios. For the same bias correction approach, in the mid-future RCP 8.5 scenario, there is an increase of 23% [14% to 31%] against 13% [4% to 33%] in the RCP 4.5 scenario, and in the far future, RX1day precipitation is projected to increase by 50% [43% to 72%] in the RCP 8.5 scenario and by 18% [7% to 36%] in the RCP 4.5 scenario. Historically, for the period of 1976-2005, no increasing trend in RX1day was observed.

An increase in precipitation extremes in the future is also evident by the increase in other indices as shown in **Table 6**. Indices like very wet days precipitation (R95pTOT), simple precipitation intensity

(SDII) and very heavy rainfall days (R20mm) are projected to increase in the mid-future and the far future for both scenarios, similarly to the RX1day and maximum 5-day (RX5day) precipitations. The increase in total annual precipitation in wet days is 3% to 37% in the future, while SDII could increase up to 30% in the far-future. The RX5day precipitation is also projected to rise between 20% and 50% in the RCP 4.5 scenario in the far future. The consecutive wet days index in RCP 4.5 scenario is projected to decrease by up to 10% in the near future but increase by up to 13 % in the far future. Similar projected changes in other river basins in Nepal like Karnali, Koshi, and Bagmati are documented in various studies (Chapagain et al., 2021; MoFE, 2019; Pandey et al., 2021; Pokharel et al., 2020; Rajbhandari et al., 2017). The only index which shows no common consensus across scenarios is the number of consecutive dry days (CDD), which could decrease or increase depending on the condition and the scenario.

Increases in rainfall variability and extremes in Kathmandu and Nepal are attributed to the Indian Summer Monsoon because it exerts major control over the overall precipitation regime (Nayava, 1980). Regional topography, i.e., the presence of the Himalaya, Middle mountains and Siwaliks, also strongly modulates the distribution of precipitation (Anders et al., 2006; Kansakar et al., 2004; Singh et al., 2019) and controls the localised extreme rainfall (Hobley et al., 2012). Hobley et al. showed that the localised convective intense rainfall, which caused widespread damage in Ladakh in 2010, occurred when the moist monsoonal air mixed with the dry Tibetan air. The projected increase in precipitation and related extremes can be attributed to the enhancement of future thermodynamic conditions leading to an increase in ISM intensity (Sharmila et al., 2015). Higher temperatures provide a conducive environment for an increase in the water-holding capacity of the air following the Clausius-Clapeyron relationship (Trenberth, 2011); higher differential temperature gradients between adjoining north Indian (including the Himalayas and Tibetan Plateau) and southern plains enhance physical processes in the region that could lead to an increase in extreme events such a convective storms (Suman and Maity, 2020).

Table 6: Predicted changes for a range of precipitation-based ETCCDI indices in the future for the Kathmandu Valley in the RCP 4.5 scenario (top) and RCP 8.5 scenario (bottom). Results shown for cold-dry, cold-wet, warm-dry and warm-wet conditions.

Indices	Unit	Observed	**Changes in RCP 4.5 scenario (%)**											
			Near Future (2015-2045)				**Mid Future (2046-2075)**				**Far Future (2076-2100)**			
		1976-2005	**cold-dry**	**cold-wet**	**warm-dry**	**warm-wet**	**cold-dry**	**cold-wet**	**warm-dry**	**warm-wet**	**cold-dry**	**cold-wet**	**warm-dry**	**warm-wet**
CDD	days	60	11	-8	21	6	-4	-13	13	-2	2	-19	0	-7
CWD	days	56	-2	-5	-10	0	-8	6	-1	10	13	11	6	11
R10mm	days	61	1	9	-7	-9	1	19	6	-4	7	14	3	-4
R20mm	days	22	8	9	-13	-11	2	27	5	5	15	16	13	3
R95pTOT	mm	357	25	20	1	22	34	52	23	34	45	31	33	45
PRCPTOT	mm	1699	2	10	-6	-3	3	21	6	4	11	17	8	5
RX1day	mm	70	8	6	11	-1	9	33	4	5	14	7	16	36
RX5day	mm	161	32	30	14	21	35	45	19	26	42	24	33	45
SDII	mm/ day	11	4	1	-2	-2	5	11	4	3	9	6	7	5
			Changes in RCP 8.5 scenario (%)											
CDD	days	60	18	-14	15	-10	5	-27	44	-8	-4	-21	23	6
CWD	days	56	15	5	2	11	1	7	7	14	-12	21	6	33
R10mm	days	61	7	12	-5	-1	4	23	-1	3	5	20	2	19
R20mm	days	22	18	16	-11	7	17	35	0	12	33	33	1	52
R95pTOT	mm	357	37	8	15	45	60	60	35	66	108	73	47	169
PRCPTOT	mm	1699	8	12	-2	7	10	26	3	12	18	28	7	37
RX1day	mm	70	-1	4	7	12	18	31	29	14	37	72	43	46
RX5day	mm	161	30	31	18	30	55	41	35	34	71	67	48	79
SDII	mm/ day	11	10	4	0	1	11	12	7	8	21	15	10	29

4.4 Quantification of rainfall extremes in terms of flood frequency and return periods

The estimates of rainfall for the return period values of 5, 10, 20, 25, 50 and 100 years for the near future (2016-2045), mid future (2046-2075) and far future (2076-2100) for RCP 4.5 and RCP 8.5 scenarios are shown in **Figure 13**. Values for a given return period for all future periods are similar, with slightly higher values for the far future compared to the mid-future and mid-future compared to the near-future. The slight variation in the results for different future periods is a result of the gentle slope of the location parameter of the generalized extreme value (GEV) distribution for the period 2006-2100. This is expected because the total time series from 2006 to 2100 was taken for non-stationary rainfall frequency analysis rather than breaking the period into specific periods. Then the return period values were estimated using a non-stationary GEV model (modelled period of 2006-2100) at the mid-point of the near-future, mid-future and far-future. From herein, results are presented for the mid-future time frame only**.** The non-stationary GEV model (NS-GEV-M1) results, where the location parameter is selected as a function of time, are used to quantify the extreme rainfall magnitudes from the frequency analysis. These results are compared to the non-stationary GEV model, where the location and shape parameters are a function of time (NS-GEV-M2), and the stationary model, where all parameters are constant in time (S – GEV). For the mid-future, rainfall values given by NS-GEV-M1 and NS-GEV-M2 are similar and slightly higher than rainfall from the stationary model S-GEV, so results from NS-GEV-M1 only are discussed further).

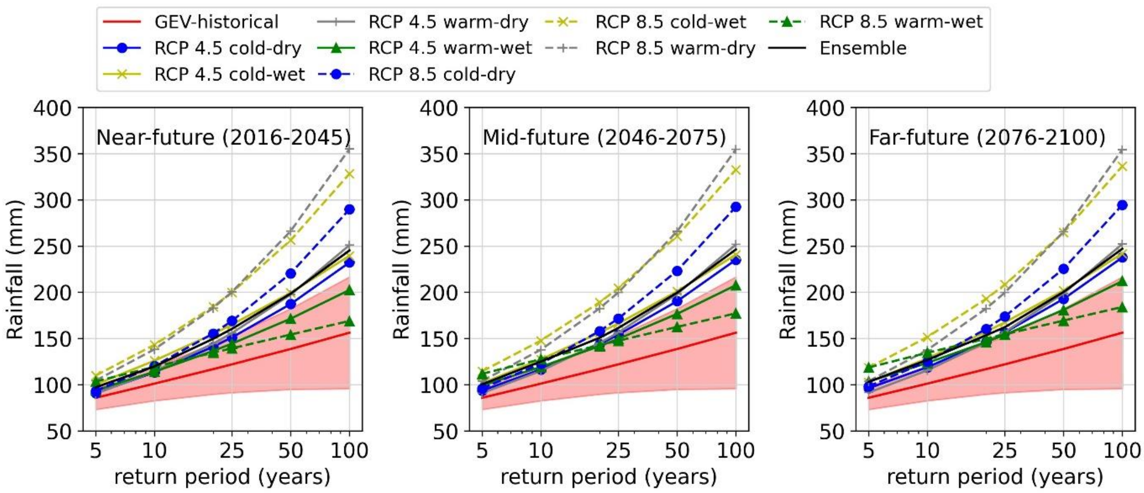

Figure 13: Rainfall frequency analysis results for different return periods in the near future, mid future and far future for a range of scenarios. The red line shows the historical GEV return periods, including the 95% confidence uncertainty band (red shaded region).

The variation of GEV parameters (location, shape and scale) in the future for the RCP 4.5 warm-wet scenario is illustrated in **Figure 14**. Figure 13 shows a linear variation of model parameters for NS-GEV-M1 and NS-GEV-M2 models because they are estimated as a function of time. As explained in section 3.6, we also used a moving window and an incremental window to understand the nature of the parameters. Wide fluctuations in the parameters can be observed when a moving window timeframe of 30 years is considered (blue dots), compared to the incremental window approach. This is expected because of the small sample size (n=30). The nature of data within the 30-year moving window time frame may also cause these fluctuations. When the sample size is increased, such as in the case of the incremental window (black dots), these parameters evolve more gradually. Scale and shape parameters showed inconsistency and fluctuations and were difficult to define (e.g. shown in **Figure 14** in RCP 4.5 warm-wet scenario). The stationary model (S-GEV-MF), which considers a shorter time frame only (e.g. 30 years for mid-future), produces unreasonably high values due to the high fluctuations in the shape parameter and, therefore, is not shown in Figure 13). Other studies have also noted the challenge of defining the shape parameter precisely, hence used a constant value (Wi et al., 2016; Committee on Adaptation to a Changing Climate, 2018; Coles, (2001)). Therefore, results from non-stationary NS-GEV-M1 were used for the flood modelling simulations, with the location parameter selected as a function of time and constant shape and scale parameters. When maximum likelihood estimates of the best-fitted line for location and shape parameters are taken into account, the variation of parameters is different because the whole future series from 2006 to 2100 was used to estimate the parameters.

Figure 14 also shows the variation of probability distribution functions based on NS-GEV-M1 in future periods and the histogram of the future RX1day precipitation. The shape parameter of GEV for RCP 8.5 WW scenario was estimated to be negative, while for the other scenarios, maximum likelihood estimates a positive shape parameter. In the RCP 8.5 WW scenario, since the shape parameter is negative, the upper bound value restricted the value of low probability values (such as the 1 in 100-year event), providing low estimates of the extreme rainfall. Therefore, the Gumbel method was adopted for RCP 8.5 warm-wet case even though its estimate is on the lower side compared to other scenarios. It is to be noted that for warm-wet case, variants of GCM are r2i1p1 for RCP 4.5 and r5i1p1 for RCP 8.5 scenario, whereas for other cases GCMs have r1i1p1 variant.

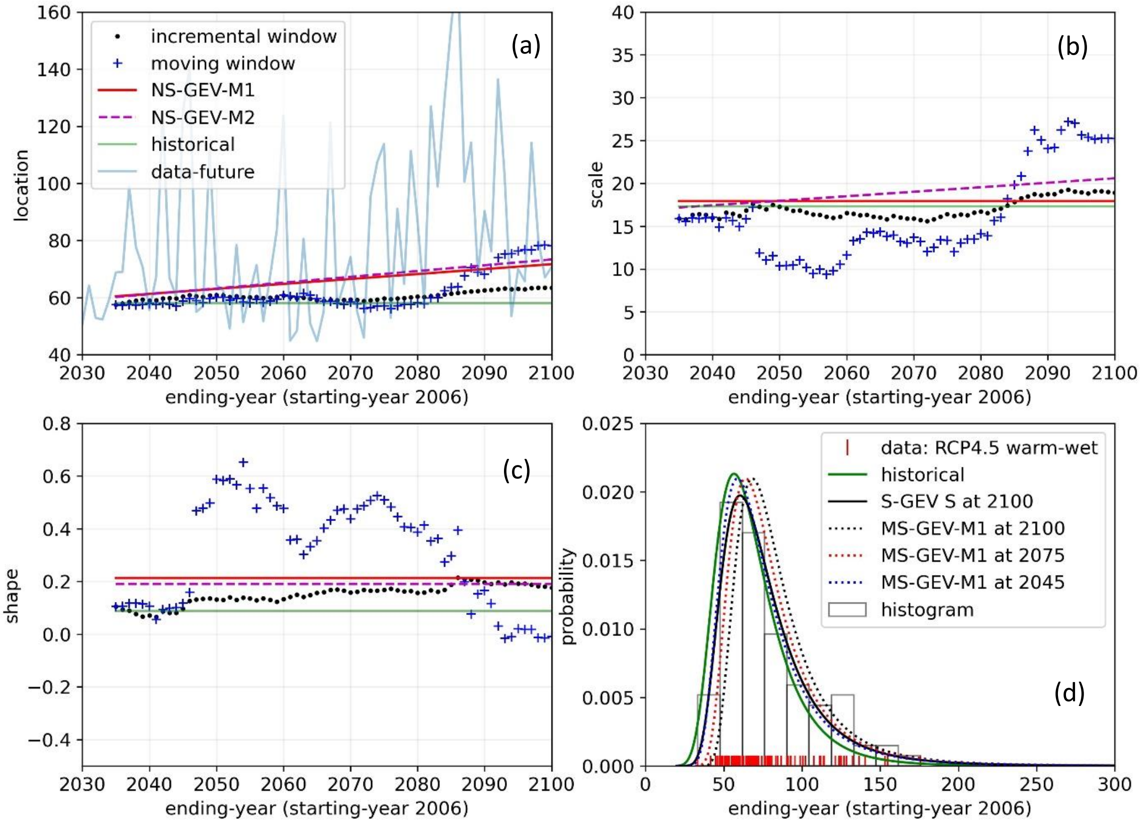

Figure 14: Variation of generalized extreme value parameters (a) location, (b) scale and (c) shape in the 2006-2100 time period and GEV curve for the RCP 4.5 warm wet scenario; (d) probability distribution function of future RX1day precipitation

Historical 100-year and 25-year return period precipitation estimates are approximately 156 mm and 122 mm, respectively, as shown in **Figure 15**. Historical return period precipitation estimate is shown by red solid line on the background of red shaded confidence interval band of 95%. The mid-future 100-year return period rainfall magnitude is projected to increase to 177mm (+13%) to 350mm (+128%), with a median projected value (considering all GCM members) of 246mm (+58%). Likewise, the mid-future 25-year return period rainfall magnitude is also expected to increase within the range of 148mm (+21%) to 204mm (+67%) with a median value of 161mm (+32%). The median line (black) shows that the historical 100-year rainfall event will be equivalent to the 25- or 20-year future rainfall event due to the increase in the intensity and frequency of rainfall extremes. Uncertainty in estimates of rainfall magnitudes is shown in the form of the error bar. Here, the uncertainty is higher for the low probability, high return period rainfall values.

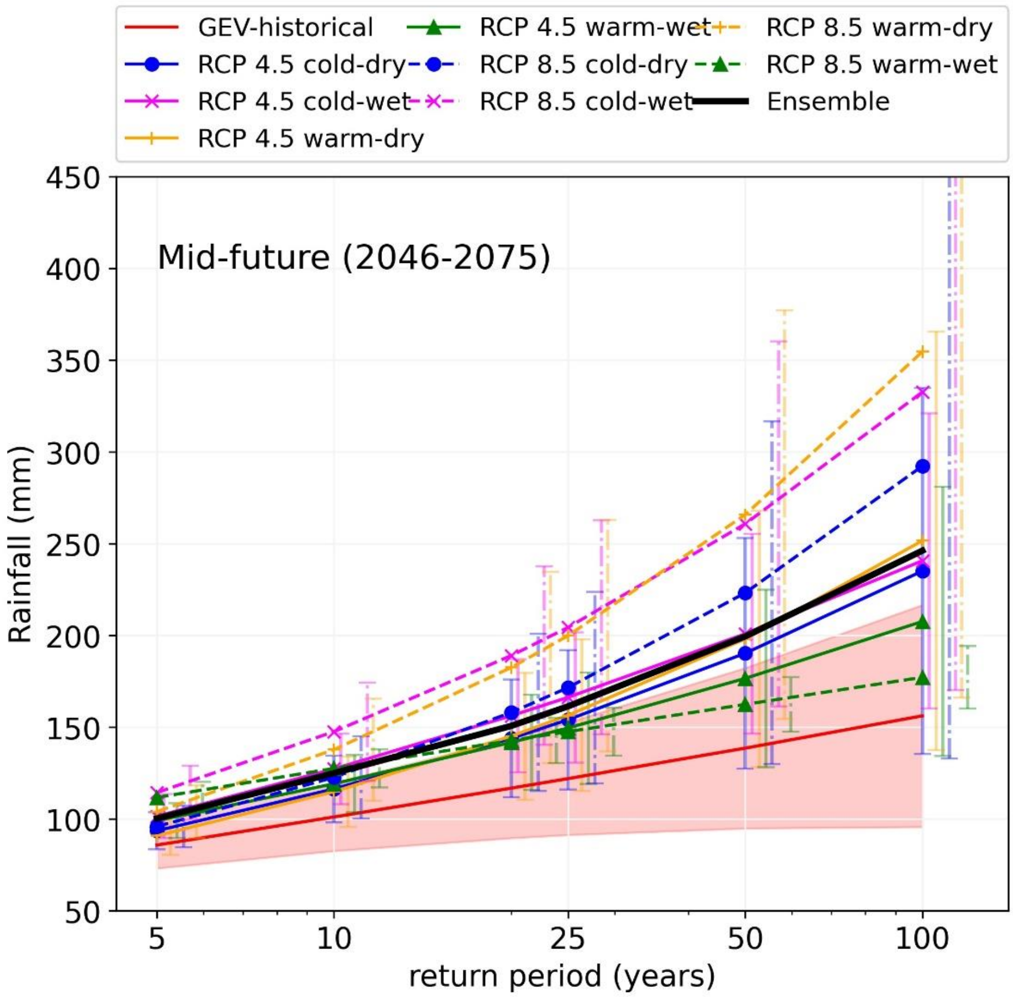

Figure 15: Estimation of projected mid-future rainfall magnitudes for different return periods and different future scenarios. Return periods based on historical rainfall extremes are shown in red with a 95% confidence interval (red shaded region).

4.5 Extreme rainfall and flood hazards

Here we present maximum inundation maps for 25-year and 100-year flood events for historical and mid-future rainfall scenarios. To simulate the flood inundation, we have applied the spatial pattern of rainfall that produced both the highest RX1day and the highest flow at Khokana (see **Figure 8**). Although the spatial distribution does affect flood inundation in different parts of the catchment differently, we base all historical and future flood models on the same rainfall distribution to allow for better comparison across flood events. Future precipitation values are chosen using RCP4.5 data only, thus more conservative than if we used the RCP8.5 data. Even so, the range of rainfall selected for the flood modelling (from 122 mm to 350 mm) covers the historical 25-year period rainfall up to the maximum mid-future 100-year return period. It also includes estimates from RCP 8.5 scenario after unrealistic values of rainfall from the rainfall-frequency analysis are excluded. Because the rainfall intensity for the RX1day historical 100-year event is equivalent to the median mid-future 25-year event (approx. 160 mm), the flood maps are almost identical. As such, RX1day flood maps will be presented for the historical 25-year and 100-year events and median and maximum mid-future 100-year events only.

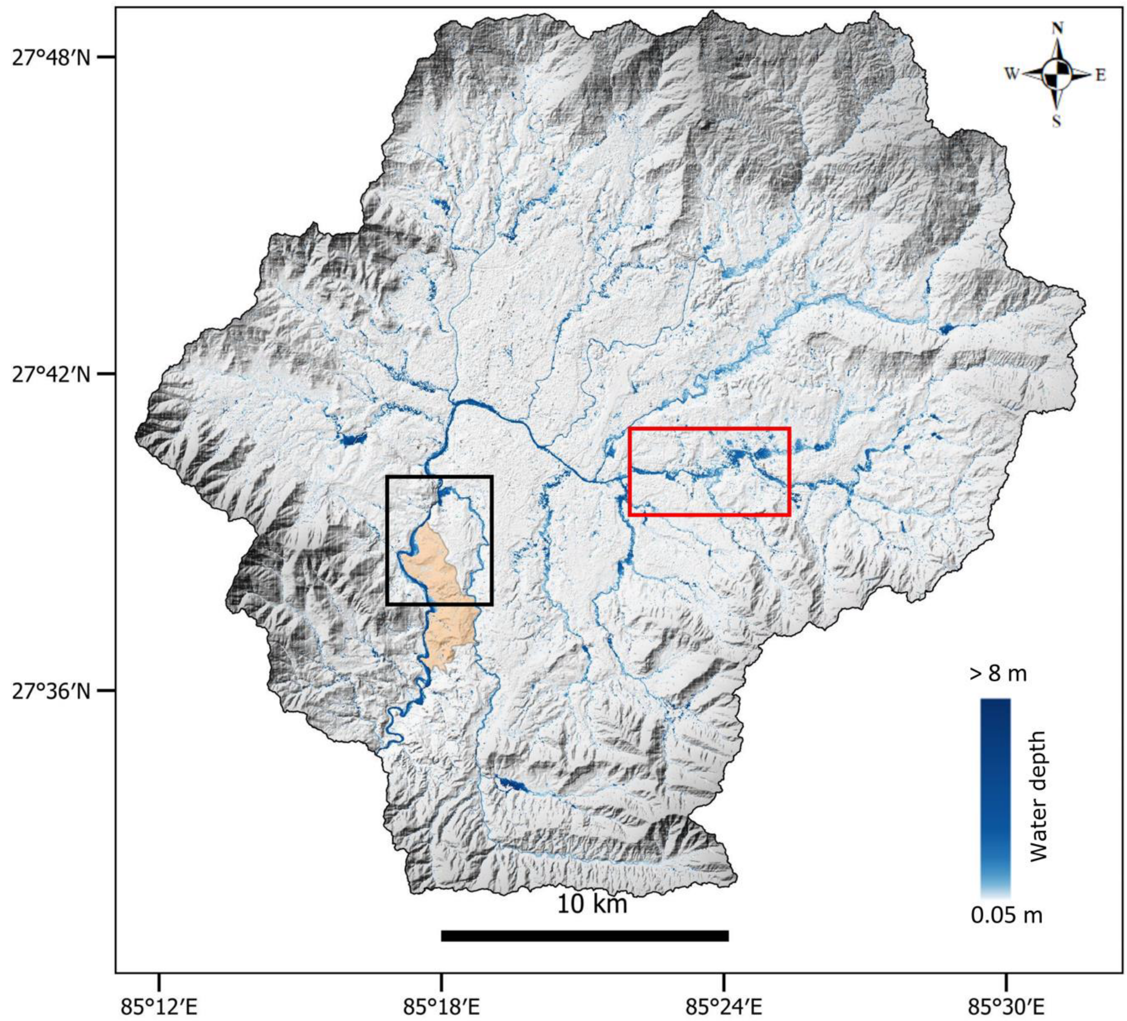

Figure 16: Flood inundation map (water depth) for the Kathmandu catchment to Khokana for the median mid-future 100-year return period rainfall event. The local regions for the Bagmati at Khokana and the Hanumante River are outlined in black and red, respectively.

Table 7 demonstrates an increase in future flood magnitudes. Compared to the historical 100-year flood, with a peak discharge of 785 m^3/s, the mid-future 100-year flood discharge is estimated to increase up to 72% (approximately 37% in the median case). A 25-year rainfall event could increase by up to 70% (approximately 26% in the median case), with a median mid-future 25-year flood magnitude higher than the historical 100-year flood magnitude. This means that the current 100-year return period flood will correspond to a 25-year period future flood at most. Besides, inundated are for water depth greater than 1m in 100-year flood will increase from 11.7 km^2 to 23 km^2. The total area inundated for each simulation is given in **Table 7**, and increases linearly with increasing rainfall intensity. An example inundation map of the Kathmandu Valley for median mid-future 100-year return period rainfall event is shown in **Figure 16**. Detailed flood maps are shown for the Bagmati at Khokana (**Figure 17**), one of the case study locations of the Tomorrow's Cities project and an area identified for future urban expansion (MoUD, 2017), and the Hanumante River (**Figure 18**), a region of the Kathmandu Valley that is prone to flood hazards. From **Figure 17** and **Figure 18,** we can see that not only does the flood extent increase, but inundation depths also increase when comparing historical and future 100-year events. The increase in depth is an important factor because depth is often used as a proxy to estimate flood damage using depth-damage curves (Dabbeek and Silva, 2020; Galasso et al., 2021). Areas which appear to receive up to 1 m of flood inundation under current climate scenarios could be inundated by over 5 m of water during future extreme events.

Table 7: Total inundation area (> 0.05 m depth) in the Kathmandu catchment in km^2 (**Figure 17**) for all scenarios modelled numerically; modelled inundation area (km^2) which has a depth greater than 1 m; simulated instantaneous maximum river depth (m) and discharge (m^3/sec) (interpolated from observed maximum instantaneous stage-discharge relationship) at the Khokana gauging station. Note that the inundation area is approximate and is affected by DEM resolution, the location of buildings, infrastructure and obstacles in the DEM, and the choice of model parameters.

Scenario	Catchment RX1day (mm)	Inundated Area (km^2)	Inundated Area for Water Depth >1 m (km^2)	Khokana Max River Depth (m)	Khokana Discharge (m^3/s)
Historical 25-year flood	122	34	9	5	632
Median mid-future 25-year flood	161	42	12.3	5.7	802
Historical 100-year flood	156	40	11.7	5.6	786
Median mid-future 100-year flood	246*	53	17.5	7	1076
Maximum mid-future 100-year flood	350	68	23	8	1356

Note * - Maximum mid-future 25-year rainfall (270 mm) is similar to median mid-future 100-year flood (246 mm), hence only the latter case is modelled numerically.

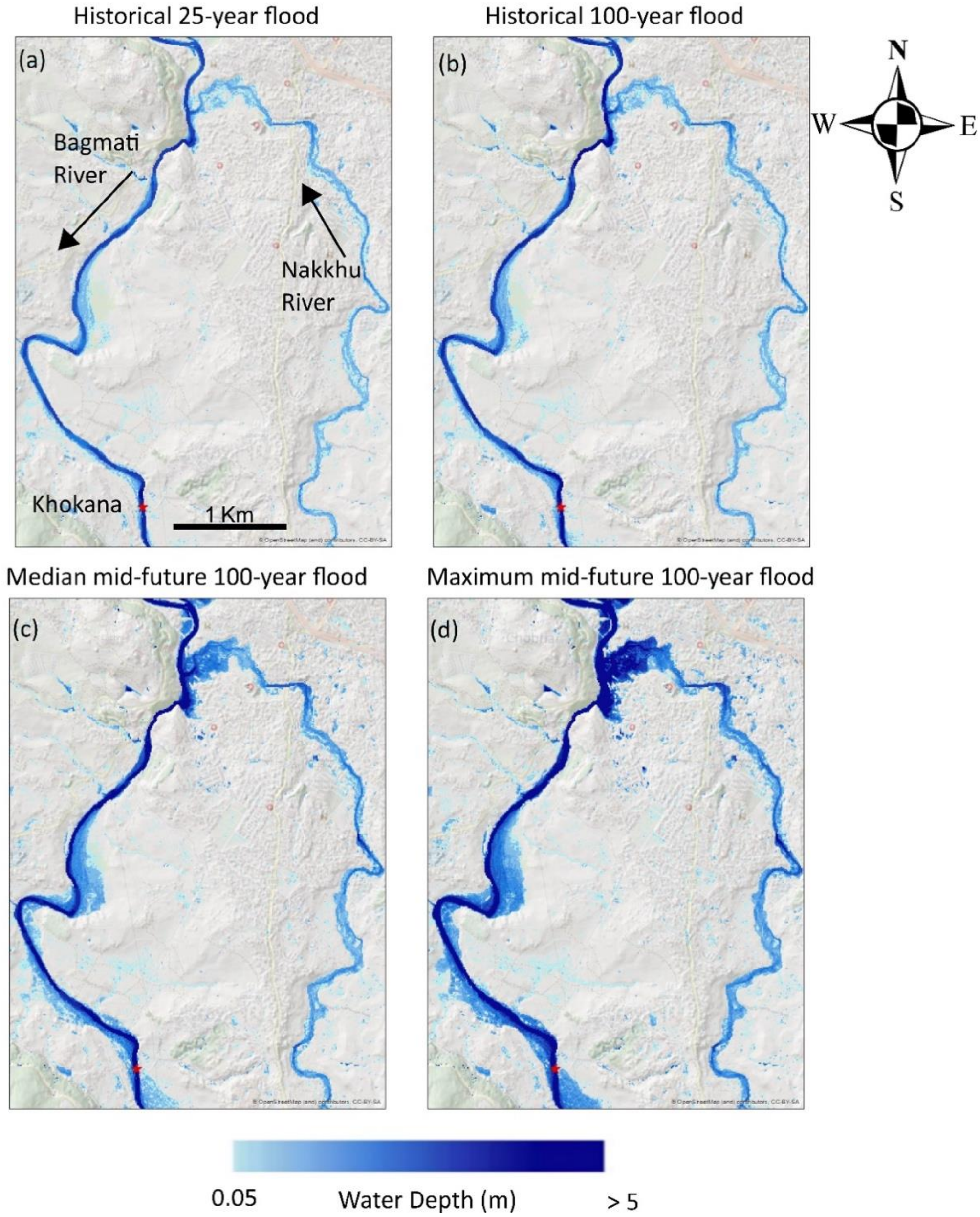

Figure 17: Flood inundation maps (water depth), generated using different rainfall intensity scenarios, for the Bagmati River and Nakkhu tributary at Khokana, which is located at the outlet of the Kathmandu valley (black rectangle shown in **Figure 16**). Black arrows represent river flow direction.

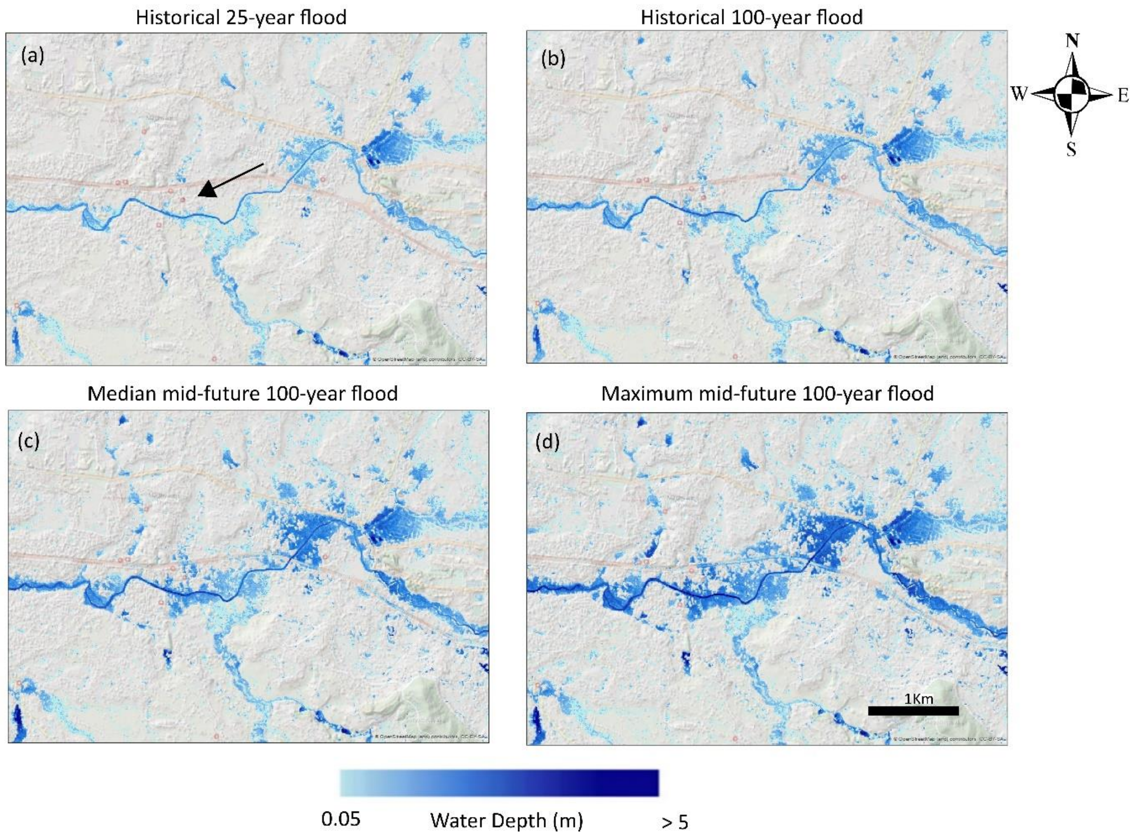

Figure 18: Flood inundation maps (water depth), generated using different rainfall intensity scenarios, for the Hanumante River (red rectangle shown in **Figure 16**). Black arrow shows river flow direction.

4.6 Uncertainties and limitations

The assessment of flood hazard in the context of climate change is influenced by various sources of uncertainty. We employed an envelope-type method (with four corners: cold-wet, cold-dry, warm-wet, and warm-dry) to represent uncertainties in estimating future floods. However, it is not necessary for the approach to encompass all aspects of uncertainty. This is because of the presence of various limitations at different stages of the method and data, which are detailed in this section.

Selection of GCM models: Precipitation uncertainty is a significant source of model uncertainty in hydrological studies (Bárdossy et al., 2022). The variations in future precipitation projections in magnitude, seasonality, and extremes by GCMs contribute significantly to this uncertainty. GCM models exhibit wide variability due to differences in parameterization of physical processes, model structure and dynamics, internal variability, initial conditions, spatial and temporal resolution, forcings, and other factors. Consequently, the selection of GCM models becomes crucial for hydrological applications.

In this study, we incorporated uncertainties by use of envelope-type method following the methods of Lutz et al. (2016) and MoFE (2019). The choice of GCMs and, consequently, the results can be influenced by different selection criteria in the model selection process. Factors such as the choice of extreme indices in step 2 or skill metrics in step 3 or even the sequence of GCM selection steps, can alter the selection outcome. Since, the projected changes in climate averages (step 1) lead the selection process, there is a narrower range of projections for climate extremes in step 2, and even fewer when assessing model runs based on their past climate performance in step 3 (Lutz et al., 2016). This could lead to the selection of GCMs that may not necessarily have fair skills in representing the past climate. Additionally, the projected changes in climate represent spatial averages across the study area, resulting in loss of information of spatial variation (Lutz et al., 2016).

The GCM selection method assumes model interdependence (Lutz et al., 2016). However, the GCMs used for selection in this study are practically not interdependent, as we employed variants of the same GCM that differ only in initial conditions. This approach may introduce additional biases. In hydrological studies, the primary source of uncertainty among various uncertainties arising from GCM models, scenarios, and ensemble members is the uncertainty associated with GCM models (Hosseinzadehtalaei et al., 2017; Wang et al., 2020; Woldemeskel et al., 2012). Restricting the selection to a single model for skill assessment could impact the results and potentially underestimate the bias to be scaled in future scenario simulations.

Bias correction: Significant biases exist in historical GCM model simulations. We applied bias correction methods to mitigate these biases, though their application may introduce additional positive or negative biases. For example, the use of quantile delta mapping increased biases in dry season precipitation. Moreover, when applying only QM or QDM without GPD-based correction for extreme values, the results could become inflated (see **Section 4.2**). Proper selection of the threshold value (in this case, the 99th percentile value of the reference period) in GPD is essential, as it affects the number of samples available for parameter estimation and, consequently, the bias correction results. Besides, trends are also not preserved by quantile mapping procedure. This stresses that the bias correction methods must be used appropriately, as they can add additional uncertainty.

Spatial and temporal sampling of observations: We conducted spatial and temporal disaggregation of future extreme values using historical rainfall patterns. Our analysis relies on a limited sample of historical extreme events (1992-2015) and we used only a common rainfall pattern in analysis of flood mapping which limits its uncertainty quantification. Furthermore, rainfall patterns beyond this timeframe might yield different flood patterns in Kathmandu. Given the short time of concentration of the Kathmandu drainage basin at Khokana, temporal distribution of sub-daily rainfall is crucial for analyzing flood peak magnitudes and occurrences. Although the GPM-IMERG final product reasonably captures spatial rainfall variation at a daily scale over Nepal (see **Section 4.1**), the performance and accuracy of temporal variation remain unexplored due to the lack of quality sub-daily scale data for Kathmandu stations. Therefore, future research should address this aspect to study the impact of temporal rainfall distribution on floods.

Rainfall-frequency analysis: Rainfall-frequency analysis for quantifying future rainfall extremes employs bias-corrected RX1day rainfall from GCMs. Naturally, uncertainties associated with GCM model selection will propagate: different choices of GCMs would yield different results. In frequency analysis, a smaller number of samples affect the estimation of GEV parameters. This is evident in the variable behavior of parameters in the moving window approach (fewer samples) compared to the stable nature of parameters in the incremental window approach (more samples) (see **Section 4.4**). Moreover, uncertainty is more pronounced for high return period rainfall. Techniques like bootstrapping methods could be explored to enhance robustness in estimating parameters and confidence intervals.

Flood hazard analysis: In flood hazard analysis, we forced the hydrodynamic model with RX1day rainfall ranging from 122 mm to 350 mm. Though the resulting discharges covers broad range of flood estimates, they may still be underestimated due to the combined impact of uncertainties related to GCM selection; bias correction; spatial/temporal sampling of observations; rainfall-frequency analysis; and hydrodynamic model inputs (e.g., DEM) and parameters (e.g., roughness coefficient, TOPMODEL parameter 'm').

5 Conclusions

Rainfall extremes for the Kathmandu Valley are projected to increase in the future across a range of scenarios. As a result, flood intensity and frequency are also expected to increase. Despite high uncertainty between different climate change projections in terms of future magnitude and frequency of rainfall intensity, our results suggest that future flood hazards will increase in the Kathmandu Valley across a range of scenarios, and future rainfall projections should be included when designing the changing landscape of this rapidly expanding urban catchment. In this study, we quantified changes in rainfall extremes in the future for Kathmandu Valley and established that the statistical properties of the rainfall will also change. We analysed the GCMs from CMIP5 in RCP 4.5 and RCP 8.5 scenarios, evaluated the historical extreme rainfall patterns that trigger floods and adopted a non-stationary rainfall frequency analysis. Our focus was on analysis and projections of the 24-hour maximum rainfall. We temporally and spatially disaggregated GPM data to an appropriate scale, as spatial and temporal distribution of rainfall directly influences the flood peak and propagation through the Kathmandu Valley.

In this study, we used the spatial rainfall pattern that generated the highest historic flood at the Khokana station when spatially distributing rainfall for the flood modelling scenarios. Different spatial distributions of future precipitation should be modelled numerically to understand the effect of future extreme rainfall events originating in the northern hills of the catchment on flood inundation and is recommended for further research.

In summary, we drew the following conclusions from this study:

(A) As indicated by extreme precipitation indices, rainfall extremes are expected to increase. The 24-hour maximum rainfall is projected to increase up to 72% depending on the future period and the scenarios considered, except for a slight decrease of 1% in the near future. This increase in rainfall directly increases the extent and magnitude of flood events.

(B) The spatial rainfall pattern needs to be considered in flood models because analysis of historical rainfall patterns shows that a concentration of rainfall maxima in the south and west part of Kathmandu causes the highest peak flood at Khokana. In addition, because the time of concentration of the catchment is about 6 hours, sub-daily rainfall should be used in flood models because this influences the peak and duration of the flood peak.

(C) Future flood magnitudes (discharge) are projected to increase in future. The mid-future 100-year flood is estimated to increase up to 72% (37% median increase) compared to the historical 100-year flood of 785 m^3/s. Similarly, the projected increase for a 25-year flood in the mid-future is up to 70% (26% median increase). Furthermore, the median mid-future 25-year flood magnitude is higher than the historical 100-year flood magnitude, meaning that the current 100-year flood will be equivalent to a 25-year future flood or a lower return period flood.

(D) Flood modelling results also show that the future flood extent (hazard) will increase with increasing rainfall and discharge magnitude. The area of land inundated by more than 1 m could increase from 11.7 km^2 to 23 km^2 between the historical 100-year return period flood and 100-year maximum mid-future flood. In addition, a change from the present day 100-year flood to a 25-year future flood means that this magnitude of the flood could become four times more likely to occur annually. This result represents an important consideration when designing future urban spaces that are resilient to floods, emphasising the need to account for future rainfall projections in all flood hazard modelling of the Kathmandu Valley.

(E) The selection of GCM models is important as it is leading the whole process. Uncertainties accumulate and propagate through bias correction, spatial/temporal disaggregation, rainfall-frequency analysis, and hydrodynamic modelling. Consequently, examining the contribution of each of these components can result in an improved estimation of uncertainties associated with future floods. Further research in these areas, therefore, will contribute to a deeper understanding of urban flood risk.

6 Declaration of Competing Interest

The authors declare that they have no known competing financial interests or personal relationships that could have appeared to influence the work reported in this paper.

7 Acknowledgements

This research was supported by UK Natural Environment Research Council Global Challenges Research Fund (GCRF) research grant - NE/S009000/1, Tomorrow's Cities Hub. We thank the Department of Hydrology and Meteorology (DHM), Nepal for providing climatic and hydrologic data.

8 References

AghaKouchak, A., Chiang, F., Huning, L.S., Love, C.A., Mallakpour, I., Mazdiyasni, O., Moftakhari, H., Papalexiou, S.M., Ragno, E., Sadegh, M., 2020. Climate Extremes and Compound Hazards in a Warming World. Annu. Rev. Earth Planet. Sci. 48, 519–548. https://doi.org/10.1146/annurev-earth-071719-055228

Alfieri, L., Bisselink, B., Dottori, F., Naumann, G., de Roo, A., Salamon, P., Wyser, K., Feyen, L., 2017. Global projections of river flood risk in a warmer world: RIVER FLOOD RISK IN A WARMER WORLD. Earths Future 5, 171–182. https://doi.org/10.1002/2016EF000485

Anders, A.M., Roe, G.H., Hallet, B., Montgomery, D.R., Finnegan, N.J., Putkonen, J., 2006. Spatial patterns of precipitation and topography in the Himalaya, in: Willett, S.D., Hovius, N., Brandon, M.T., Fisher, D.M. (Eds.), Tectonics, Climate, and Landscape Evolution. Geological Society of America, p. 0. https://doi.org/10.1130/2006.2398(03)

Aryal, R.K., Lee, B.-K., Karki, R., Gurung, A., Kandasamy, J., Pathak, B.K., Sharma, S., Giri, N., 2008. Seasonal PM10 dynamics in Kathmandu Valley. Atmos. Environ. 42, 8623–8633. https://doi.org/10.1016/j.atmosenv.2008.08.016

Bárdossy, A., Kilsby, C., Birkinshaw, S., Wang, N., Anwar, F., 2022. Is Precipitation Responsible for the Most Hydrological Model Uncertainty? Front. Water 4, 836554. https://doi.org/10.3389/frwa.2022.836554

Basnyat, D.B., Shrestha, D., Thapa, S., Bajimaya, S., Maharjan, M., Shrestha, S., Dhungana, S., 2020. Post-Flood Assessment: Case Study of the 2019 Flooding in Bagmati Basin. J. Dev. Innov. 4, 20–47.

Bates, P.D., Horritt, M.S., Fewtrell, T.J., 2010. A simple inertial formulation of the shallow water equations for efficient two-dimensional flood inundation modelling. J. Hydrol. 387, 33–45. https://doi.org/10.1016/j.jhydrol.2010.03.027

Beven, K.J., Kirkby, M.J., 1979. A physically based, variable contributing area model of basin hydrology / Un modèle à base physique de zone d'appel variable de l'hydrologie du bassin versant. Hydrol. Sci. Bull. 24, 43–69. https://doi.org/10.1080/02626667909491834

Bohlinger, P., Sorteberg, A., Sodemann, H., 2017. Synoptic Conditions and Moisture Sources Actuating Extreme Precipitation in Nepal. J. Geophys. Res. Atmospheres 122. https://doi.org/10.1002/2017JD027543

Bookhagen, B., Burbank, D.W., 2006. Topography, relief, and TRMM-derived rainfall variations along the Himalaya. Geophys. Res. Lett. 33, L08405. https://doi.org/10.1029/2006GL026037

Brown, C., Boltz, F., Freeman, S., Tront, J., Rodriguez, D., 2020. Resilience by design: A deep uncertainty approach for water systems in a changing world. Water Secur. 9, 100051. https://doi.org/10.1016/j.wasec.2019.100051

Brunner, M.I., Slater, L., Tallaksen, L.M., Clark, M., 2021. Challenges in modeling and predicting floods and droughts: A review. WIREs Water 8. https://doi.org/10.1002/wat2.1520

Cannon, A.J., Sobie, S.R., Murdock, T.Q., 2015. Bias Correction of GCM Precipitation by Quantile Mapping: How Well Do Methods Preserve Changes in Quantiles and Extremes? J. Clim. 28, 6938–6959. https://doi.org/10.1175/JCLI-D-14-00754.1

Chapagain, D., Dhaubanjar, S., Bharati, L., 2021. Unpacking future climate extremes and their sectoral implications in western Nepal. Clim. Change 168, 8. https://doi.org/10.1007/s10584-021-03216-8

Chow, V.T., Maidment, D.R., Mays, L.W., 1988. Applied Hydrology. McGraw-Hill, New York.

Clark, M.P., Fan, Y., Lawrence, D.M., Adam, J.C., Bolster, D., Gochis, D.J., Hooper, R.P., Kumar, M., Leung, L.R., Mackay, D.S., Maxwell, R.M., Shen, C., Swenson, S.C., Zeng, X., 2015. Improving the representation of hydrologic processes in Earth System Models: REPRESENTING HYDROLOGIC PROCESSES IN EARTH SYSTEM MODELS. Water Resour. Res. 51, 5929–5956. https://doi.org/10.1002/2015WR017096

Coles, S., 2001. An introduction to statistical modeling of extreme values, Springer Series in Statistics. Springer-Verlag, London.

Committee on Adaptation to a Changing Climate, 2018. Climate-Resilient Infrastructure: Adaptive Design and Risk Management. American Society of Civil Engineers, Reston, VA. https://doi.org/10.1061/9780784415191

Coulthard, T.J., Macklin, M.G., Kirkby, M.J., 2002. A cellular model of Holocene upland river basin and alluvial fan evolution. Earth Surf. Process. Landf. 27, 269–288. https://doi.org/10.1002/esp.318

Coulthard, T.J., Neal, J.C., Bates, P.D., Ramirez, J., de Almeida, G.A.M., Hancock, G.R., 2013. Integrating the LISFLOOD-FP 2D hydrodynamic model with the CAESAR model: implications for modelling landscape evolution. Earth Surf. Process. Landf. 38, 1897–1906. https://doi.org/10.1002/esp.3478

Cremen, G., Galasso, C., McCloskey, J., 2022. Modelling and quantifying tomorrow's risks from natural hazards. Sci. Total Environ. 817, 152552. https://doi.org/10.1016/j.scitotenv.2021.152552

Cremen, G., Galasso, C., McCloskey, J., Barcena, A., Creed, M., Filippi, M.E., Gentile, R., Jenkins, L.T., Kalaycioglu, M., Mentese, E.Y., Muthusamy, M., Tarbali, K., Trogrlić, R.Š., 2023. A state-of-the-art decision-support environment for risk-sensitive and pro-poor urban planning and design in Tomorrow's cities. Int. J. Disaster Risk Reduct. 85, 103400. https://doi.org/10.1016/j.ijdrr.2022.103400

Dabbeek, J., Silva, V., 2020. Modeling the residential building stock in the Middle East for multi-hazard risk assessment. Nat. Hazards 100, 781–810. https://doi.org/10.1007/s11069-019-03842-7

Dodman, D., Hayward, B., Pelling, M., Castan Broto, V., Chow, W., Chu, E., Dawson, R., Khirfan, L., McPhearson, T., Prakash, A., Zheng, Y., Ziervogel, G., 2022. Cities, Settlements and Key Infrastructure. In: Climate Change 2022: Impacts, Adaptation, and Vulnerability. Contribution of Working Group II to the Sixth Assessment Report of the Intergovernmental Panel on Climate Change [H.-O. Pörtner, D.C. Roberts, M. Tignor, E.S. Poloczanska, K. Mintenbeck, A. Alegría, M. Craig, S. Langsdorf, S. Löschke, V. Möller, A. Okem, B. Rama (eds.)].

Dottori, F., Alfieri, L., Bianchi, A., Skoien, J., Salamon, P., 2022. A new dataset of river flood hazard maps for Europe and the Mediterranean Basin. Earth Syst Sci Data 14, 1549–1569. https://doi.org/10.5194/essd-14-1549-2022

Feeney, C.J., Chiverrell, R.C., Smith, H.G., Hooke, J.M., Cooper, J.R., 2020. Modelling the decadal dynamics of reach-scale river channel evolution and floodplain turnover in CAESAR-Lisflood. Earth Surf. Process. Landf. 45, 1273–1291. https://doi.org/10.1002/esp.4804

Finger, D., Heinrich, G., Gobiet, A., Bauder, A., 2012. Projections of future water resources and their uncertainty in a glacierized catchment in the Swiss Alps and the subsequent effects on hydropower production during the 21st century: PROJECTIONS OF FUTURE WATER RESOURCES. Water Resour. Res. 48. https://doi.org/10.1029/2011WR010733

Fowler, H.J., Blenkinsop, S., Tebaldi, C., 2007. Linking climate change modelling to impacts studies: recent advances in downscaling techniques for hydrological modelling: ADVANCES IN DOWNSCALING TECHNIQUES FOR HYDROLOGICAL MODELLING. Int. J. Climatol. 27, 1547–1578. https://doi.org/10.1002/joc.1556

Galasso, C., McCloskey, J., Pelling, M., Hope, M., Bean, C.J., Cremen, G., Guragain, R., Hancilar, U., Menoscal, J., Mwang'a, K., Phillips, J., Rush, D., Sinclair, H., 2021. Editorial. Risk-based, Pro-poor Urban Design and Planning for Tomorrow's Cities. Int. J. Disaster Risk Reduct. 58, 102158. https://doi.org/10.1016/j.ijdrr.2021.102158

Gudmundsson, L., Bremnes, J.B., Haugen, J.E., Engen-Skaugen, T., 2012. Technical Note: Downscaling RCM precipitation to the station scale using statistical transformations – a comparison of methods. Hydrol Earth Syst Sci 16, 3383–3390. https://doi.org/10.5194/hess-16-3383-2012

Hakala, K., Addor, N., Teutschbein, C., Vis, M., Dakhlaoui, H., Seibert, J., 2019. Hydrological Modeling of Climate Change Impacts, in: Maurice, P. (Ed.), Encyclopedia of Water. Wiley, pp. 1–20. https://doi.org/10.1002/9781119300762.wsts0062

Herschy, R. W., Marsh, T.J., Herschy, R. W., Schumann, A.H., 1998. Thiessen PolygonThiessen polygon, in: Herschy, Reginald W., Fairbridge, R.W. (Eds.), Encyclopedia of Hydrology and Water Resources. Springer Netherlands, Dordrecht, pp. 648–649. https://doi.org/10.1007/978-1-4020-4497-7_220

Hobley, D.E.J., Sinclair, H.D., Mudd, S.M., 2012. Reconstruction of a major storm event from its geomorphic signature: The Ladakh floods, 6 August 2010. Geology 40, 483–486. https://doi.org/10.1130/G32935.1

Hosseinzadehtalaei, P., Tabari, H., Willems, P., 2017. Uncertainty assessment for climate change impact on intense precipitation: how many model runs do we need?: UNCERTAINTY OF CLIMATE CHANGE IMPACT ON INTENSE PRECIPITATION. Int. J. Climatol. 37, 1105–1117. https://doi.org/10.1002/joc.5069

Huffman, G.J., Stocker, E.F., Bolvin, D.T., Nelkin, E.J., Tan, J., 2019. GPM IMERG Final Precipitation L3 Half Hourly 0.1 degree x 0.1 degree V06. Greenbelt MD Goddard Earth Sci. Data Inf. Serv. Cent. GES DISC.

IPCC, 2022. Summary for Policymakers [H.-O. Pörtner, D.C. Roberts, E.S. Poloczanska, K. Mintenbeck, M. Tignor, A. Alegría, M. Craig, S. Langsdorf, S. Löschke, V. Möller, A. Okem (eds.)]. In: Climate Change 2022: Impacts, Adaptation, and Vulnerability. Contribution of Working Group II to the Sixth Assessment Report of the Intergovernmental Panel on Climate Change [H.-O. Pörtner, D.C. Roberts, M. Tignor, E.S. Poloczanska, K. Mintenbeck, A. Alegría, M. Craig, S. Langsdorf, S. Löschke, V. Möller, A. Okem, B. Rama (eds.)]. Cambridge University Press. In Press.

Jenkins, L.T., Creed, M.J., Tarbali, K., Muthusamy, M., Trogrlić, R.Š., Phillips, J.C., Watson, C.S., Sinclair, H.D., Galasso, C., McCloskey, J., 2023. Physics-based simulations of multiple natural hazards for risk-sensitive planning and decision making in expanding urban regions. Int. J. Disaster Risk Reduct. 84, 103338. https://doi.org/10.1016/j.ijdrr.2022.103338

Kaini, S., Nepal, S., Pradhananga, S., Gardner, T., Sharma, A.K., 2021. Impacts of climate change on the flow of the transboundary Koshi River, with implications for local irrigation. Int. J. Water Resour. Dev. 37, 929–954. https://doi.org/10.1080/07900627.2020.1826292

Kansakar, S.R., Hannah, D.M., Gerrard, J., Rees, G., 2004. Spatial pattern in the precipitation regime of Nepal. Int. J. Climatol. 24, 1645–1659. https://doi.org/10.1002/joc.1098

Kirpich, Z.P., 1940. Time of concentration of small agricultural watersheds. Civ. Eng. 10, 362.

Lamichhane, S., Shakya, N.M., 2019. Alteration of groundwater recharge areas due to land use/cover change in Kathmandu Valley, Nepal. J. Hydrol. Reg. Stud. 26, 100635. https://doi.org/10.1016/j.ejrh.2019.100635

Lutz, A.F., ter Maat, H.W., Biemans, H., Shrestha, A.B., Wester, P., Immerzeel, W.W., 2016. Selecting representative climate models for climate change impact studies: an advanced envelope-based selection approach. Int. J. Climatol. 36, 3988–4005. https://doi.org/10.1002/joc.4608

Malgwi, M.B., Ramirez, J.A., Zischg, A., Zimmermann, M., Schürmann, S., Keiler, M., 2021. A method to reconstruct flood scenarios using field interviews and hydrodynamic modelling: application to the 2017 Suleja and Tafa, Nigeria flood. Nat. Hazards 108, 1781–1805. https://doi.org/10.1007/s11069-021-04756-z

Maraun, D., 2013. Bias Correction, Quantile Mapping, and Downscaling: Revisiting the Inflation Issue. J. Clim. 26, 2137–2143. https://doi.org/10.1175/JCLI-D-12-00821.1

Milly, P.C.D., Betancourt, J., Falkenmark, M., Hirsch, R.M., Kundzewicz, Z.W., Lettenmaier, D.P., Stouffer, R.J., 2008. Stationarity Is Dead: Whither Water Management? Science 319, 573–574. https://doi.org/10.1126/science.1151915

Minville, M., Brissette, F., Leconte, R., 2008. Uncertainty of the impact of climate change on the hydrology of a nordic watershed. J. Hydrol. 358, 70–83. https://doi.org/10.1016/j.jhydrol.2008.05.033

MoFE, 2021. Vulnerability and risk assessment and identifying adaptation options in the water resources and energy in Nepal: Sectoral report water resources and energy.

MoFE, 2019. Climate change scenarios for Nepal for National Adaptation Plan (NAP).

MoUD, 2017. National Urban Development Strategy (NUDS), 2017 Part A Main Document.

Nayava, J.L., 1980. Rainfall in Nepal. Himal. Rev. 12, 1–18.

Neal, J., Villanueva, I., Wright, N., Willis, T., Fewtrell, T., Bates, P., 2012. How much physical complexity is needed to model flood inundation? Hydrol. Process. 26, 2264–2282. https://doi.org/10.1002/hyp.8339

Nepal, B., Shrestha, D., Sharma, S., Shrestha, M.S., Aryal, D., Shrestha, N., 2021. Assessment of GPM-Era Satellite Products' (IMERG and GSMaP) Ability to Detect Precipitation Extremes over Mountainous Country Nepal. Atmosphere 12, 254. https://doi.org/10.3390/atmos12020254

Ojha, A., 2021. Encroachment of Kathmandu Valley's rivers and poor drainage worsen inundation.

Ojha, A., Dhungana, S., 2021. Not just rains, poor urban planning causing flash floods in Kathmandu.

Pandey, V.P., Dhaubanjar, S., Bharati, L., Thapa, B.R., 2020. Spatio-temporal distribution of water availability in Karnali-Mohana Basin, Western Nepal: Climate change impact assessment (Part-B). J. Hydrol. Reg. Stud. 29, 100691. https://doi.org/10.1016/j.ejrh.2020.100691

Pandey, V.P., Shrestha, D., Adhikari, M., 2021. Characterizing natural drivers of water-induced disasters in a rain-fed watershed: Hydro-climatic extremes in the Extended East Rapti Watershed, Nepal. J. Hydrol. 598, 126383. https://doi.org/10.1016/j.jhydrol.2021.126383

Pokharel, A.K., Hallett, J., 2015. Distribution of rainfall intensity during the summer monsoon season over Kathmandu, Nepal. Weather 70, 257–261. https://doi.org/10.1002/wea.2544

Pokharel, B., Wang, S.-Y.S., Meyer, J., Marahatta, S., Nepal, B., Chikamoto, Y., Gillies, R., 2020. The east–west division of changing precipitation in Nepal. Int. J. Climatol. 40, 3348–3359. https://doi.org/10.1002/joc.6401

Ragno, E., AghaKouchak, A., Love, C.A., Cheng, L., Vahedifard, F., Lima, C.H.R., 2018. Quantifying Changes in Future Intensity-Duration-Frequency Curves Using Multimodel Ensemble Simulations. Water Resour. Res. 54, 1751–1764. https://doi.org/10.1002/2017WR021975

Rajbhandari, R., Shrestha, A.B., Nepal, S., Wahid, S., Ren, G.-Y., 2017. Extreme climate projections over the transboundary Koshi River Basin using a high resolution regional climate model. Spec. Issue Clim. Change Hindu Kush Himalaya 8, 199–211. https://doi.org/10.1016/j.accre.2017.08.006

Richardson, K.J., 2021. Extreme precipitation events in South Asia: understanding climate drivers through case studies. UK Met Office, Exeter, UK.

Richter, I., Chang, P., Liu, X., 2020. Impact of Systematic GCM Errors on Prediction Skill as Estimated by Linear Inverse Modeling. J. Clim. 33, 10073–10095. https://doi.org/10.1175/JCLI-D-20-0209.1

Roe, G.H., 2005. OROGRAPHIC PRECIPITATION. Annu. Rev. Earth Planet. Sci. 33, 645–671. https://doi.org/10.1146/annurev.earth.33.092203.122541

Sharma, S., Khadka, N., Hamal, K., Shrestha, D., Talchabhadel, R., Chen, Y., 2020. How Accurately Can Satellite Products (TMPA and IMERG) Detect Precipitation Patterns, Extremities, and Drought Across the Nepalese Himalaya? Earth Space Sci. 7. https://doi.org/10.1029/2020EA001315

Sharmila, S., Joseph, S., Sahai, A.K., Abhilash, S., Chattopadhyay, R., 2015. Future projection of Indian summer monsoon variability under climate change scenario: An assessment from CMIP5 climate models. Glob. Planet. Change 124, 62–78. https://doi.org/10.1016/j.gloplacha.2014.11.004

Shrestha, M., Acharya, S.C., 2021. Assessment of historical and future land-use–land-cover changes and their impact on valuation of ecosystem services in Kathmandu Valley, Nepal. Land Degrad. Dev. 32, 3731–3742. https://doi.org/10.1002/ldr.3837

Sillmann, J., Kharin, V.V., Zhang, X., Zwiers, F.W., Bronaugh, D., 2013a. Climate extremes indices in the CMIP5 multimodel ensemble: Part 1. Model evaluation in the present climate. J. Geophys. Res. Atmospheres 118, 1716–1733. https://doi.org/10.1002/jgrd.50203

Sillmann, J., Kharin, V.V., Zwiers, F.W., Zhang, X., Bronaugh, D., 2013b. Climate extremes indices in the CMIP5 multimodel ensemble: Part 2. Future climate projections. J. Geophys. Res. Atmospheres 118, 2473–2493. https://doi.org/10.1002/jgrd.50188

Singh, D., Ghosh, S., Roxy, M.K., McDermid, S., 2019. Indian summer monsoon: Extreme events, historical changes, and role of anthropogenic forcings. WIREs Clim. Change 10, e571. https://doi.org/10.1002/wcc.571

Stephenson, A.G., Heffernan, J.E., Gilleland, E., 2018. ismev: An Introduction to Statistical Modeling of Extreme Values.

Suman, M., Maity, R., 2020. Southward shift of precipitation extremes over south Asia: Evidences from CORDEX data. Sci. Rep. 10, 6452. https://doi.org/10.1038/s41598-020-63571-x

Talchabhadel, R., Karki, R., 2019. Assessing climate boundary shifting under climate change scenarios across Nepal. Environ. Monit. Assess. 191, 520. https://doi.org/10.1007/s10661-019-7644-4

Talchabhadel, R., Shah, S., Aryal, B., 2022. Evaluation of the Spatiotemporal Distribution of Precipitation Using 28 Precipitation Indices and 4 IMERG Datasets over Nepal. Remote Sens. 14, 5954. https://doi.org/10.3390/rs14235954

Tank, A.M.G.K., Zwiers, F.W., Zhang, X., 2009. Climate data and monitoring WCDMP-No. 72 - Guidelines on analysis of extremes in a changing climate in support of informed decisions for adaptatio.

Teutschbein, C., Seibert, J., 2012. Bias correction of regional climate model simulations for hydrological climate-change impact studies: Review and evaluation of different methods. J. Hydrol. 456–457, 12–29. https://doi.org/10.1016/j.jhydrol.2012.05.052

Themeßl, M.J., Gobiet, A., Heinrich, G., 2012. Empirical-statistical downscaling and error correction of regional climate models and its impact on the climate change signal. Clim. Change 112, 449–468. https://doi.org/10.1007/s10584-011-0224-4

Thiessen, A.H., 1911. Precipitation for large areas Monthly Weather Rev. Vol. 39. Julio Httpsdoi Org1011751520-0493 1911 39, 1082–1084.

Trenberth, K., 2011. Changes in precipitation with climate change. Clim. Res. 47, 123–138. https://doi.org/10.3354/cr00953

Uprety, M., 2019. A dramatic start to Nepal's 2019 monsoon season. URL https://floodresilience.net/blogs/a-dramatic-start-to-nepals-2019-monsoon-season/ (accessed 3.1.22).

Valters, D.A., 2017. Modelling catchment sensitivity to rainfall resolution and erosional parameterisation in simulations of flash floods in the UK. The University of Manchester, Manchester, UK.

van Vuuren, D.P., Edmonds, J., Kainuma, M., Riahi, K., Thomson, A., Hibbard, K., Hurtt, G.C., Kram, T., Krey, V., Lamarque, J.-F., Masui, T., Meinshausen, M., Nakicenovic, N., Smith, S.J., Rose, S.K., 2011. The representative concentration pathways: an overview. Clim. Change 109, 5. https://doi.org/10.1007/s10584-011-0148-z

Wang, H., Chen, J., Xu, C., Zhang, J., Chen, H., 2020. A Framework to Quantify the Uncertainty Contribution of GCMs Over Multiple Sources in Hydrological Impacts of Climate Change. Earths Future 8. https://doi.org/10.1029/2020EF001602

Whetton, P., Hennessy, K., Clarke, J., McInnes, K., Kent, D., 2012. Use of Representative Climate Futures in impact and adaptation assessment. Clim. Change 115, 433–442. https://doi.org/10.1007/s10584-012-0471-z

Wi, S., Valdés, J.B., Steinschneider, S., Kim, T.-W., 2016. Non-stationary frequency analysis of extreme precipitation in South Korea using peaks-over-threshold and annual maxima. Stoch. Environ. Res. Risk Assess. 30, 583–606. https://doi.org/10.1007/s00477-015-1180-8

Wilson, C.B., Valdes, J.B., Rodriguez-Iturbe, I., 1979. On the influence of the spatial distribution of rainfall on storm runoff. Water Resour. Res. 15, 321–328. https://doi.org/10.1029/WR015i002p00321

Woldemeskel, F.M., Sharma, A., Sivakumar, B., Mehrotra, R., 2012. An error estimation method for precipitation and temperature projections for future climates: QUANTIFYING GCMS OUTPUT UNCERTAINTY. J. Geophys. Res. Atmospheres 117, n/a-n/a. https://doi.org/10.1029/2012JD018062

Yin, M., Han, Y., Wang, Y., Sun, W., Deng, J., Wei, D., Kong, Y., Wang, B., 2023. Climate impacts of parameterizing subgrid variation and partitioning of land surface heat fluxes to the atmosphere with the NCAR CESM1.2. Geosci Model Dev 16, 135–156. https://doi.org/10.5194/gmd-16-135-2023

Zoccatelli, D., Borga, M., Viglione, A., Chirico, G.B., Blöschl, G., 2011. Spatial moments of catchment rainfall: rainfall spatial organisation, basin morphology, and flood response. Hydrol Earth Syst Sci 15, 3767–3783. https://doi.org/10.5194/hess-15-3767-2011

Shrestha, D. et al. (2023) Rainfall extremes under future climate change with implications for urban flood risk in Kathmandu, Nepal. *International Journal of Disaster Risk Reduction*, 97, 103997.

(doi: 10.1016/j.ijdrr.2023.103997)

This is the author accepted manuscript. There may be differences between this version and the published version. You are advised to consult the published version if you wish to cite from it:
https://doi.org/10.1016/j.ijdrr.2023.103997

© 2023 Elsevier Ltd. Reproduced under a Creative Commons Attribution Noncommercial-Noderivatives 4.0 International Licence.

Enlighten record available at: https://eprints.gla.ac.uk/346499/

Deposited on 23 May 2025

Enlighten – Research publications by members of the University of Glasgow

https://eprints.gla.ac.uk